
Coupling fluid-structure interaction with phase-field fracture

Thomas Wick

Johann Radon Institute for Computational
and Applied Mathematics (RICAM)
Austrian Academy of Sciences
Altenberger Str. 69
4040 Linz, Austria

Accepted for publication in
Journal of Computational Physics (JCP)
in Sep 2016

DOI: <https://doi.org/10.1016/j.jcp.2016.09.024>
©2016. This manuscript version is made available under the
CC-BY-NC-ND 4.0 license
<https://creativecommons.org/licenses/by-nc-nd/4.0/>

Coupling fluid-structure interaction with phase-field fracture

Thomas Wick^{a,1}

^a*Johann Radon Institute for Computational and Applied Mathematics (RICAM)*
Austrian Academy of Sciences, Altenberger Str. 69, 4040 Linz, Austria

Abstract

In this work, a concept for coupling fluid-structure interaction with brittle fracture in elasticity is proposed. The fluid-structure interaction problem is modeled in terms of the arbitrary Lagrangian-Eulerian technique and couples the isothermal, incompressible Navier-Stokes equations with nonlinear elastodynamics using the Saint-Venant Kirchhoff solid model. The brittle fracture model is based on a phase-field approach for cracks in elasticity and pressurized elastic solids. In order to derive a common framework, the phase-field approach is re-formulated in Lagrangian coordinates to combine it with fluid-structure interaction. A crack irreversibility condition, that is mathematically characterized as an inequality constraint in time, is enforced with the help of an augmented Lagrangian iteration. The resulting problem is highly nonlinear and solved with a modified Newton method (e.g., error-oriented) that specifically allows for a temporary increase of the residuals. The proposed framework is substantiated with several numerical tests. In these examples, computational stability in space and time is shown for several goal functionals, which demonstrates reliability of numerical modeling and algorithmic techniques. But also current limitations such as the necessity of using solid damping are addressed.

Keywords: fluid-structure interaction, arbitrary Lagrangian-Eulerian technique, pressurized phase-field fracture, dynamic brittle fracture, augmented Lagrangian approach, finite elements

2000 MSC: 2010 74R10; 74F10; 65M60; 49M15; 35Q74

1. Introduction

Both fluid-structure interaction (FSI) and fracture propagation are current but challenging topics with numerous applications in applied mathematics and engineering. For FSI literature we exemplary refer to the books [17, 33, 36, 16, 8] and for fracture mechanics we refer to [42, 67, 71, 82, 4, 12, 70]; and references cited therein are also emphasized. The goal of this work is to bring both frameworks together. This is of great interest since often FSI settings should also be able to account for fracture (or damage) of the solid part. On the other hand, single or multiple fractures or fracture networks can be found, for instance, in geomechanics, geophysics and porous media, which are possibly filled with fluids or coupled to surrounding flow. Thus, a framework that contains elastodynamics (which do also allow to account for large solid deformations), fluid flow, and a model for fracture representation and propagation is of current interest.

In classical FSI, the isothermal, incompressible Navier-Stokes equations are coupled with elastodynamics. The constitutive law in the solid is based on the geometrically nonlinear Saint-Venant Kirchhoff (STVK) model, see e.g., [20]. Here, three unknowns are sought: velocities, pressure and displacements. The FSI coupling technique is based on an interface-tracking method; namely the nowadays standard arbitrary Lagrangian-Eulerian (ALE) technique [25, 47, 50, 63, 32]. Here, the flow equations are re-written such that their coordinate system matches the Lagrangian framework of the solid. The resulting formulation using variational-monolithic coupling in the reference configuration is outlined in [49, 68, 74]. The key feature of the ALE approach is that the interface aligns with mesh edges and therefore interface-terms such as traction forces can be computed with high accuracy. In addition, it allows for many settings up to large solid deformations as long as the ALE mapping is a C^1 -diffeomorphism.

Email address: thomas.wick@ricam.oeaw.ac.at (Thomas Wick)

On the other hand, brittle fracture propagation using variational techniques has attracted attention in recent years since the pioneering work in [35, 11]. Since in FSI the constitutive stress tensor is generally nonlinear, we also refer to [21] who formulated quasistatic fracture growth using a variational setting employing nonlinear elasticity. The numerical approach [11] is based on Ambrosio-Tortorelli elliptic functionals [2, 3]. Here, discontinuities in the displacement field across the lower-dimensional crack surface are approximated by an auxiliary function φ . This function can be viewed as an indicator function, which introduces a diffusive transition zone between the broken and the unbroken material. This zone has a half bandwidth ε , which is a model regularization parameter. From an application viewpoint, two situations are of interest for given fracture(s): first, observing the variation of the fracture width (crack opening displacement) and second, change of the fracture length. The latter situation is by far more complicated. However, both configurations are of importance and variational fracture techniques can be used for both of them.

Fracture evolutions satisfy a crack irreversibility constraint such that the resulting system can be characterized as a variational inequality. Our motivation for employing such a variational approach is that fracture nucleation, propagation, kinking, and curvilinear paths are automatically included in the model. In addition, explicit remeshing or reconstruction of the crack path is not necessary. The underlying equations are based on continuum mechanics principles that can be treated with (adaptive) Galerkin finite elements. On the contrary the underlying energy functional is not simultaneously convex in both solution variables [35] and a crucial difficulty. Another challenge is the resolution of ε in relation to the spatial discretization parameter $h < \varepsilon$, which requires local mesh adaptivity around the crack zone [43] when very small ε are of interest as well as a posteriori error estimation [5] and goal functional evaluations [79]; otherwise the computational cost becomes prohibitive.

An important modification of [35] towards a thermodynamically-consistent phase-field fracture (PFF) model has been accomplished in [59, 56]. This approach has been extended to pressurized fractures in [61, 62]. Here, the crack irreversibility constraint has been imposed through penalization. In phase-field fracture, two unknowns are sought: displacements and a phase-field function that determines the crack location. Recent advances and numerical studies towards pressurized and fluid-filled fracture and other multiphysics applications including thermo-elastic-plastic solids and coupling with a reservoir simulator have been considered in [62, 60, 73, 58, 55, 80]. However, to the best of our knowledge coupling with classical FSI and the need to work with different coordinate systems has not yet been considered, which constitutes a major novelty of the present work.

As previously described, the solid part of FSI is based on elastodynamics, and therefore we accentuate the work of [9, 52, 13, 51] who extended variational quasi-static brittle fracture to dynamic brittle fracture taking into account the solid acceleration term. Moreover, the authors of [52] introduced an elastic dissipation term, which is for wave propagation problems known as strong solid damping. This term improves the regularity of the solid velocity, see e.g., [37]. In the analysis for dynamic fracture this term was crucial, see [52][Remark 2.2], the corresponding theorems, and their conclusions. It turns out that in our numerical simulations we also need such a term; specifically for fractures that increase not only their width but also their length.

The goal in this paper is to couple ALE fluid-structure interaction with pressurized phase-field fracture. In order to achieve this task, we combine four models:

1. Nonlinear ALE fluid-structure interaction;
2. Crack representation and propagation in elastodynamics with phase-field;
3. Enforcing crack irreversibility via an augmented Lagrangian technique;
4. Pressurized phase-field fracture modeling in Lagrangian coordinates in a fixed reference domain.

In the first model, we deal with three types of nonlinearities: fluid convection, a geometrically nonlinear Green-Lagrange strain tensor, and finally the nonlinear ALE mapping. With regard to the second approach, we emphasize that we consider fixed fractures that only vary in their width as well as the more challenging configuration of propagating fractures. The third model does not need further comments and follows the ideas originally proposed in [34, 40]. The fourth approach has been worked out for quasi-static fractures in porous media [61, 62]. In the present work, this idea is extended to dynamic fractures in solid mechanics. The phase-field fracture equation is formulated in Lagrangian coordinates in order to match them with the ALE prescription of fluid-structure interaction.

The resulting formulation is consequently prescribed in a fixed, but arbitrary, reference domain and all coupling conditions are satisfied in a variational exact fashion on the continuous level. This formulation is now fully-coupled and can be written in terms of a Galerkin form. Then, numerical discretization is straightforward as the Rothe method

(first time, then space) can be applied on the resulting semilinear form. These steps will be explained in great detail. The discretized, nonlinear coupled problem is solved with Newton's method with a modification that allows for an increase of the residual. This can be achieved either with an error-oriented line-search globalization [24] or simply using a classical residual-based approach that sometimes violates the convergence criterion.

In summary, the novelties in this paper are three-fold:

1. A phase-field model for (propagating) pressurized dynamic fracture(s);
2. Coupling of FSI and phase-field fracture, i.e., formulating phase-field in terms of ALE coordinates in order to match fluid-structure interaction modeling, which also includes careful modeling of interface conditions;
3. A-stable time-stepping and higher order spatial discretization for solving transient fluid-structure interaction and satisfying the inf-sup condition of the Navier-Stokes flow. These numerical developments are then demonstrated through systematic qualitative convergence studies while demonstrating computational stability in time and space for the coupled FSI-PFF system.

The outline of this paper is as follows: In Section 2, the notation, spaces and all basic equations are gathered. In the following Section 3 an augmented Lagrangian formulation of the final problem is presented. Next in Section 4, details on the discretization and the solution algorithms are discussed. Several numerical tests in Section 5 are consulted to investigate the proposed framework. Here, the focus is on goal functional evaluations in order to show computational stability in space and time. First results for moderate flow and small deformations are published in [77].

2. Notation, spaces, and equations for fluids, solids, and fracture

2.1. Notation

We denote by $\Omega := \Omega(t) \subset \mathbb{R}^d$, $d = 2$, the domain of the FSI phase-field fracture problem; see Figure 1. The domain consists of three time-dependent subdomains $\Omega_f(t)$, $\Omega_s(t)$ and $C(t)$. We assume $C(t) \subset\subset \Omega_s(t)$. The FSI-interface between $\Omega_f(t)$ and $\Omega_s(t)$ is denoted by $\Gamma_i(t) = \partial\Omega_f(t) \cap \partial\Omega_s(t)$. The initial (or later reference) domains are denoted by $\widehat{\Omega}$, $\widehat{\Omega}_f$ and $\widehat{\Omega}_s$, respectively, with the interface $\widehat{\Gamma}_i = \partial\widehat{\Omega}_f \cap \partial\widehat{\Omega}_s$. Furthermore, we denote the outer boundary by $\partial\widehat{\Omega} = \widehat{\Gamma} = \widehat{\Gamma}_{in} \cup \widehat{\Gamma}_D \cup \widehat{\Gamma}_{out}$ where $\widehat{\Gamma}_D$ and $\widehat{\Gamma}_{in}$ are Dirichlet boundaries (for the velocities and displacements) and $\widehat{\Gamma}_{out}$ denotes a fluid outflow Neumann boundary, respectively. The displacements are set to zero on $\widehat{\Gamma}_{out}$.

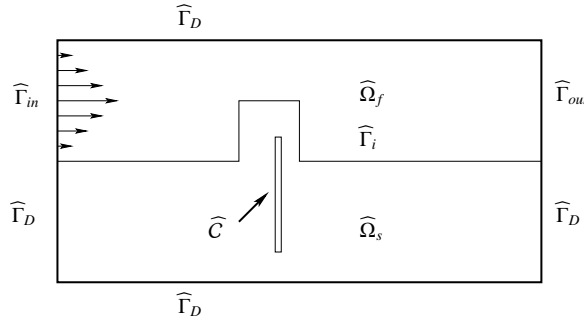


Figure 1: Notation of domains and boundaries.

As frequently used in the literature, we denote the L^2 scalar product in Ω with $(a, b) := (a, b)_\Omega := \int_\Omega a \cdot b \, dx$ for vectors a, b . For (2nd order) tensor-valued functions A, B , it yields $(A, B) := (A, B)_\Omega := \int_\Omega A : B \, dx$, where $A : B = \sum_{ij=1}^d A_{ij}B_{ij}$ and A_{ij} and B_{ij} are the entries of A and B .

2.2. Spaces

For the function spaces in the (fixed) reference domains $\widehat{\Omega}$, $\widehat{\Omega}_f$, $\widehat{\Omega}_s$, \widehat{C} , we define spaces for spatial discretization only. Rather than employing Bochner-spaces [22, 81] for space-time functions, the time t is later explicitly accounted

for, e.g., [29] (Section 7.1). Here, let $I := [0, T]$ be the time interval and T the end time value. In the fluid domain, we work with

$$\begin{aligned}\hat{L}_f &:= L^2(\widehat{\Omega}_f), \\ \hat{L}_f^0 &:= L^2(\widehat{\Omega}_f)/\mathbb{R}, \\ \hat{V}_f^0 &:= \{\hat{v}_f \in H^1(\widehat{\Omega}_f)^d : \hat{v}_f = 0 \text{ on } \widehat{\Gamma}_{in} \cup \widehat{\Gamma}_D\}, \\ \hat{V}_{f,\hat{u}}^0 &:= \{\hat{u}_f \in H^1(\widehat{\Omega}_f)^d : \hat{u}_f = \hat{u}_s \text{ on } \widehat{\Gamma}_i, \quad \hat{u}_f = 0 \text{ on } \widehat{\Gamma}_{in} \cup \widehat{\Gamma}_D \cup \widehat{\Gamma}_{out}\}, \\ \hat{V}_{f,\hat{u},\widehat{\Gamma}_i}^0 &:= \{\hat{\psi}_f \in H^1(\widehat{\Omega}_f)^d : \hat{\psi}_f = 0 \text{ on } \widehat{\Gamma}_i \cup \widehat{\Gamma}_{in} \cup \widehat{\Gamma}_D \cup \widehat{\Gamma}_{out}\}.\end{aligned}$$

In the solid domain, we work with

$$\begin{aligned}\hat{L}_s &:= L^2(\widehat{\Omega}_s)^d, \\ \hat{V}_s^0 &:= \{\hat{u}_s \in H^1(\widehat{\Omega}_s)^d : \hat{u}_s = 0 \text{ on } \widehat{\Gamma}_D\}, \\ \hat{W} &:= \{\hat{\varphi} \in H^1(\widehat{\Omega}_s \cup \widehat{C}) : \hat{\varphi} \leq \hat{\varphi}^{old} \text{ a.e. on } \widehat{\Omega}_s \cup \widehat{C}\}.\end{aligned}$$

In the last space $\hat{\varphi}^{old}$ will later represent the previous time step solution of the phase-field variable. Moreover, in the presence of a fracture \widehat{C} inside the solid domain $\widehat{\Omega}_s$ the solid function spaces are extended to hold for functions defined in $\widehat{\Omega}_s \cup \widehat{C}$.

For the FSI problem using variational-monolithic coupling [49, 27, 28] the velocity spaces are extended from $\widehat{\Omega}_f$ and $\widehat{\Omega}_s$ to the entire domain $\widehat{\Omega}$ such that we can work with global H^1 functions. Thus, we define:

$$\hat{V}^0 := \{\hat{v} \in H^1(\widehat{\Omega})^d : \hat{v} = 0 \text{ on } \widehat{\Gamma}_{in} \cup \widehat{\Gamma}_D\}. \quad (1)$$

By this choice, the kinematic and dynamic coupling conditions are automatically satisfied in a variational sense. Alternative definitions with a similar aim can be found, for example, in [30, 31, 15].

Finally, we notice that the spaces on the current domains $\Omega, \Omega_f, \Omega_s, C$ are defined correspondingly without ‘hat’ notation.

2.3. The ALE concept, transformed fluid flow, and solids in Lagrangian coordinates

In this section, we recapitulate the ingredients to formulate a coupled problem (i.e., fluid-structure interaction) with the help of the ALE approach. The ALE mapping $\hat{\mathcal{A}} : \widehat{\Omega}_f \rightarrow \Omega_f$ is defined first. The corresponding solid transformation $\widehat{T} : \widehat{\Omega}_s \rightarrow \Omega_s$ is later used to transform phase-field on a reference configuration.

2.3.1. The ALE transformation and ALE time-derivative

First, we define the ALE transformation:

Definition 2.1. The ALE mapping is defined in terms of the vector-valued (artificial) fluid mesh displacement $\hat{u}_f : \widehat{\Omega}_f \rightarrow \mathbb{R}^d$ such that

$$\hat{\mathcal{A}}(\hat{x}, t) : \widehat{\Omega}_f \times I \rightarrow \Omega_f, \quad \text{with } \hat{\mathcal{A}}(\hat{x}, t) = \hat{x} + \hat{u}_f(\hat{x}, t), \quad (2)$$

which is specified through the deformation gradient and its determinant

$$\widehat{F} := \widehat{\nabla} \hat{\mathcal{A}} = \hat{I} + \widehat{\nabla} \hat{u}_f, \quad \hat{J} := \det(\widehat{F}). \quad (3)$$

Furthermore, function values in Eulerian and Lagrangian coordinates are identified by

$$u_f(x) =: \hat{u}_f(\hat{x}), \quad \text{with } x = \hat{\mathcal{A}}(\hat{x}, t). \quad (4)$$

Here, \hat{I} denotes the identity matrix. The mesh velocity is defined by $\hat{w} := \partial_t \hat{\mathcal{A}}$. The key quantity to measure the fluid mesh regularity is \hat{J} . The artificial fluid displacement \hat{u}_f (the mesh motion) is obtained in this work by solving an additional partial differential equation for mesh moving. Various possibilities are presented in [44, 72, 74, 26]. Finally, the transformation between different coordinate systems requires transformation of derivatives. For a vector-valued function $u \in \Omega$ and $\hat{u} \in \widehat{\Omega}$ it holds, e.g., [48]:

$$\nabla u = \widehat{\nabla} \hat{u} \widehat{F}^{-1}.$$

Finally, the ALE time-derivative is the total derivative of an Eulerian field and is important when working on moving domains:

$$\partial_t|_{\mathcal{A}} v_f(x, t) = \hat{w} \cdot \nabla v_f + \partial_t v_f(x, t). \quad (5)$$

2.4. Equations for fluids and solids

In this section, we briefly state the basic underlying equations first separately. This illustrates in a clear way that the solid equations serve as the complementary part to the FSI problem, stated in Section 2.5, but the same solid equations are used in the phase-field fracture formulation presented in Section 2.6. In the following, we first present fluid flow and then the solid part.

2.4.1. Strong forms

The isothermal, incompressible Navier-Stokes equations in an ALE setting read: Find $v_f : \Omega_f(t) \times I \rightarrow \mathbb{R}^d$ and $p_f : \Omega_f(t) \times I \rightarrow \mathbb{R}$ such that

$$\begin{aligned} \rho_f \partial_t|_{\mathcal{A}} v_f + \rho_f (v_f - \hat{w}) \cdot \nabla v_f - \nabla \cdot \sigma_f(v_f, p_f) &= 0, & \nabla \cdot v_f &= 0 \quad \text{in } \Omega_f(t), \\ v_f^D &= v_{in} \text{ on } \Gamma_{in}, & v_f &= 0 \text{ on } \Gamma_D, & -p_f n_f + \rho_f v_f \nabla v_f \cdot n_f &= 0 \text{ on } \Gamma_{out}, & v_f &= h_f \text{ on } \Gamma_i, \\ v_f(0) &= v_0 \text{ in } \Omega_f(0), \end{aligned}$$

where the (symmetric) Cauchy stress is given by

$$\sigma_f(v_f, p_f) := -pI + \rho_f v_f (\nabla v + \nabla v^T),$$

with the density ρ_f and the kinematic viscosity ν_f . Later in the FSI problem, the function h_f will be given by the solid velocity v_s . The normal vector is denoted by n_f .

The equations for geometrically non-linear elastodynamics are given as follows: Find $\hat{u}_s : \widehat{\Omega}_s \times I \rightarrow \mathbb{R}^d$ such that

$$\begin{aligned} \hat{\rho}_s \partial_t^2 \hat{u}_s - \widehat{\nabla} \cdot (\widehat{F} \widehat{\Sigma}) - \partial_t \widehat{\nabla} \cdot (\widehat{\Sigma}_v) &= 0 \quad \text{in } \widehat{\Omega}_s, \\ \hat{u}_s &= 0 \text{ on } \widehat{\Gamma}_D, & (\widehat{F} \widehat{\Sigma} + \partial_t \widehat{\Sigma}_v) \cdot \hat{n}_s &= \hat{h}_s \text{ on } \widehat{\Gamma}_i, \\ \hat{u}_s(0) &= \hat{u}_0 \text{ in } \widehat{\Omega}_s \times \{0\}, & \hat{v}_s(0) &= \hat{v}_0 \text{ in } \widehat{\Omega}_s \times \{0\}. \end{aligned}$$

The constitutive laws are given by the tensors:

$$\widehat{\Sigma} = \widehat{\Sigma}_s(\hat{u}_s) = 2\mu \widehat{E} + \lambda \text{tr}(\widehat{E})I, \quad \widehat{E} = \frac{1}{2}(\widehat{F}^T \widehat{F} - I), \quad (6)$$

$$\widehat{\Sigma}_v = \widehat{\Sigma}_v(\hat{u}_s) = 2\mu_v \widehat{E}_{lin} + \lambda_v \text{tr}(\widehat{E}_{lin})I, \quad \widehat{E}_{lin} = \frac{1}{2}(\widehat{\nabla} \hat{u}_s + \widehat{\nabla} \hat{u}_s^T). \quad (7)$$

Here, μ and λ are the Lamé coefficients for the solid and μ_v and λ_v are constants in the solid damping term. The solid density is denoted by $\hat{\rho}_s$ and the solid deformation gradient is $\widehat{F} = \widehat{I} + \widehat{\nabla} \hat{u}_s$. Later in FSI, the vector-valued function \hat{h}_s will be given by the normal stress from the fluid problem. Furthermore, \hat{n}_s denotes the normal vector.

Remark 2.1. Since solid damping is linear it holds

$$\partial_t \widehat{\Sigma}_v(\hat{u}_s) = \widehat{\Sigma}_v(\hat{v}_s) = 2\mu_v \widehat{E}_{lin}(\hat{v}_s) + \lambda_v \text{tr}(\widehat{E}_{lin}(\hat{v}_s))I, \quad \partial_t \widehat{E}_{lin}(\hat{u}_s) = \widehat{E}_{lin}(\hat{v}_s) = \frac{1}{2}(\widehat{\nabla} \hat{v}_s + \widehat{\nabla} \hat{v}_s^T).$$

2.4.2. Variational forms

The previous Navier-Stokes equations in a variational ALE framework described in a reference domain $\widehat{\Omega}_f$ are given by:

Formulation 1 (ALE Navier-Stokes in $\widehat{\Omega}_f$). Let \widehat{v}_f^D a suitable extension of Dirichlet inflow data. Find vector-valued velocities and a scalar-valued pressure $\{\widehat{v}_f, \widehat{p}_f\} \in \{\widehat{v}_f^D + \widehat{V}_f^0\} \times \widehat{L}_f^0$ such that the initial data $\widehat{v}_f(0) = \widehat{v}_f^0$ are satisfied, and for almost all times $t \in I$ holds:

$$\begin{aligned} \widehat{\rho}_f(\widehat{J}\partial_t \widehat{v}_f, \widehat{\psi}_f^v)_{\widehat{\Omega}_f} + \widehat{\rho}_f(\widehat{J}\widehat{F}^{-1}(\widehat{v}_f - \widehat{w}) \cdot \widehat{\nabla} \widehat{v}_f, \widehat{\psi}_f^v)_{\widehat{\Omega}_f} + (\widehat{J}\widehat{\sigma}_f \widehat{F}^{-T}, \widehat{\nabla} \widehat{\psi}_f^v)_{\widehat{\Omega}_f} \\ - \langle \widehat{J}\widehat{g}_f \widehat{F}^{-T} \widehat{n}_f, \widehat{\psi}_f^v \rangle_{\widehat{\Gamma}_{out}} - \langle \widehat{J}\widehat{\sigma}_f \widehat{F}^{-T} \widehat{n}_f, \widehat{\psi}_f^v \rangle_{\widehat{\Gamma}_i} = 0 \quad \forall \widehat{\psi}_f^v \in \widehat{V}_f^0, \\ (\widehat{\operatorname{div}}(\widehat{J}\widehat{F}^{-1}\widehat{v}_f), \widehat{\psi}_f^p)_{\widehat{\Omega}_f} = 0 \quad \forall \widehat{\psi}_f^p \in \widehat{L}_f^0. \end{aligned}$$

Here, $\widehat{g}_f := -\widehat{\rho}_f v_f \widehat{F}^{-T} \widehat{\nabla} \widehat{v}_f^T$ denotes a correction term on the outflow boundary (see Remark 2.2) and \widehat{n}_f is the outer normal vector. The transformed Cauchy stress tensor reads:

$$\widehat{\sigma}_f = -\widehat{p}_f \widehat{I} + 2\widehat{\rho}_f v_f (\widehat{\nabla} \widehat{v}_f \widehat{F}^{-1} + \widehat{F}^{-T} \widehat{\nabla} \widehat{v}_f^T). \quad (8)$$

Remark 2.2 (Do-nothing fluid outflow condition on $\widehat{\Gamma}_{out}$). Due to the choice of the function spaces of the variational fluid Formulation 1 (namely not imposing any conditions for the velocity on the outlet $\widehat{\Gamma}_{out}$) a natural boundary condition of Neumann type is automatically contained in the variational formulation. This is the so-called ‘do-nothing’ condition [46] since nothing needs to be done to prescribe this condition. Concretely, the do-nothing condition yields parallel streamlines on the outflow boundary in channel flow with parabolic inflow. Furthermore, this condition yields a unique pressure since the normalization

$$\int_{\widehat{\Gamma}_{out}} \widehat{p}_f d\widehat{s} = 0, \quad (9)$$

is implicitly contained in the do-nothing condition; for details we refer the reader to [46] and [66]. However, the do-nothing condition has been derived for Navier-Stokes flow with non-symmetric stress tensor $\sigma_f = -p_f I + \rho_f v_f (\nabla v_f)$. When working with symmetric fluid stresses (which is necessary for the conservation of angular momentum), a ‘correction term’ can be imposed on the outflow boundary in order to keep parallel streamlines on the outlet. This correction term is again a Neumann condition and reads in ALE coordinates: $-\langle \widehat{J}\widehat{g}_f \widehat{F}^{-T} \widehat{n}_f, \widehat{\psi}_f^v \rangle_{\widehat{\Gamma}_{out}}$.

The variational formulation for elastodynamics can be formulated as a first-order-in-time system:

Formulation 2 (First order system in time weak formulation of elasticity including strong damping). Find $\widehat{u}_s \in \widehat{V}_s^0$ and $\widehat{v}_s \in \widehat{L}_s$ with the initial data $\widehat{u}_s(0) = \widehat{u}_0$ and $\widehat{v}_s(0) = \widehat{v}_0$ such that for almost all times $t \in I$:

$$\begin{aligned} \widehat{\rho}_s(\partial_t \widehat{v}_s, \widehat{\psi}_s^v)_{\widehat{\Omega}_s} + (\widehat{F}\widehat{\Sigma}, \widehat{\nabla} \widehat{\psi}_s^v)_{\widehat{\Omega}_s} + (\partial_t \widehat{\Sigma}_v(\widehat{u}_s), \widehat{\nabla} \widehat{\psi}_s^v)_{\widehat{\Omega}_s} \\ - \langle \widehat{F}\widehat{\Sigma} \widehat{n}_s, \widehat{\psi}_s^v \rangle_{\widehat{\Gamma}_i} - \langle \partial_t \widehat{\Sigma}_v \widehat{n}_s, \widehat{\psi}_s^v \rangle_{\widehat{\Gamma}_i} = 0 \quad \forall \widehat{\psi}_s^v \in \widehat{V}_s^0, \\ \widehat{\rho}_s(\partial_t \widehat{u}_s - \widehat{v}_s, \widehat{\psi}_s^u)_{\widehat{\Omega}_s} = 0 \quad \forall \widehat{\psi}_s^u \in \widehat{L}_s. \end{aligned}$$

2.5. Variational-monolithic ALE fluid-structure interaction (yet without fractures)

2.5.1. FSI interface coupling conditions

The coupling of a fluid with a solid must satisfy two physical conditions; namely continuity of velocities and continuity of normal stresses. A third condition of geometric nature is necessary when working with the ALE framework: continuity of displacements, which couples the physical solid \widehat{u}_s and the fluid mesh motion \widehat{u}_f . Mathematically, the first and third conditions can be classified as (non-homogeneous) Dirichlet conditions and the second condition is a (non-homogeneous) Neumann condition.

In variational-monolithic coupling these Dirichlet conditions are built into the corresponding function space by employing a globalized Sobolev space \widehat{V}^0 (see (1)). Neumann type conditions are weakly incorporated through interface integrals, which actually cancel out in the later models because of their weak continuity thanks to working with the space \widehat{V}^0 .

For the fluid problem, continuity of velocities is required (i.e., a kinematic coupling condition):

$$v_f = v_s \quad \text{on } \Gamma_i. \quad (10)$$

To complete the solid problem, we must enforce the balance of the normal stresses on the interface (i.e., a dynamic coupling condition):

$$\hat{J}\hat{\sigma}_f\hat{F}^{-T}\hat{n}_f + \hat{F}\hat{\Sigma}\hat{n}_s + \hat{\Sigma}_v(\hat{v})\hat{n}_s = 0 \quad \text{on } \hat{\Gamma}_i. \quad (11)$$

For the geometric problem we have

$$u_f = u_s \quad \text{on } \Gamma_i, \quad (12)$$

from which we obtain immediately $\partial_t u_s = v_s = w = v_f$ on Γ_i by temporal differentiation.

2.5.2. The FSI model

The weak form of a variational-monolithic FSI model using nonlinear harmonic mesh motion reads, e.g., [27, 74]:

Formulation 3 (Variational-monolithic ALE fluid-structure interaction in $\widehat{\Omega}$). Find a global vector-valued velocity, vector-valued displacements and a scalar-valued fluid pressure, i.e., $\{\hat{v}, \hat{u}_f, \hat{u}_s, \hat{p}_f\} \in \{\hat{v}^D + \hat{V}^0\} \times \{\hat{u}_f^D + \hat{V}_{f,\hat{u}}^0\} \times \{\hat{u}_s^D + \hat{V}_s^0\} \times \hat{L}_f^0$, such that $\hat{v}(0) = \hat{v}^0$, $\hat{u}_f(0) = \hat{u}_f^0$, and $\hat{u}_s(0) = \hat{u}_s^0$ are satisfied, and for almost all times $t \in I$ holds:

$$\begin{aligned} \text{Fluid/solid momentum} & \left\{ \begin{array}{l} (\hat{J}\hat{\rho}_f\partial_t\hat{v}, \hat{\psi}^v)_{\widehat{\Omega}_f} + (\hat{\rho}_f\hat{J}(\hat{F}^{-1}(\hat{v} - \hat{w}) \cdot \hat{\nabla})\hat{v}, \hat{\psi}^v)_{\widehat{\Omega}_f} + (\hat{J}\hat{\sigma}_f\hat{F}^{-T}, \hat{\nabla}\hat{\psi}^v)_{\widehat{\Omega}_f} \\ + \langle \hat{\rho}_f v_f \hat{J}(\hat{F}^{-T}\hat{\nabla}\hat{v}^T\hat{n}_f) \hat{F}^{-T}, \hat{\psi}^v \rangle_{\widehat{\Gamma}_{out}} \\ + (\hat{\rho}_s\partial_t\hat{v}, \hat{\psi}^v)_{\widehat{\Omega}_s} + (\hat{F}\hat{\Sigma}, \hat{\nabla}\hat{\psi}^v)_{\widehat{\Omega}_s} + (\hat{\Sigma}_v(\hat{v}), \hat{\nabla}\hat{\psi}^v)_{\widehat{\Omega}_s} = 0 \quad \forall \hat{\psi}^v \in \hat{V}^0, \end{array} \right. \\ \text{Fluid mesh motion} & \left\{ (\widehat{\sigma}_{mesh}, \hat{\nabla}\hat{\psi}_f^u)_{\widehat{\Omega}_f} = 0 \quad \forall \hat{\psi}_f^u \in \hat{V}_{f,\hat{u},\widehat{\Gamma}_i}^0, \right. \\ \text{Solid momentum, 2nd eq.} & \left\{ \hat{\rho}_s(\partial_t\hat{u}_s - \hat{v}|_{\widehat{\Omega}_s}, \hat{\psi}_s^u)_{\widehat{\Omega}_s} = 0 \quad \forall \hat{\psi}_s^u \in \hat{L}_s, \right. \\ \text{Fluid mass conservation} & \left. \left\{ (\widehat{\operatorname{div}}(\hat{J}\hat{F}^{-1}\hat{v}), \hat{\psi}_f^p)_{\widehat{\Omega}_f} = 0 \quad \forall \hat{\psi}_f^p \in \hat{L}_f^0. \right. \right. \end{aligned}$$

The stress tensors for fluid and solid have been discussed before. The constitutive law for the mesh motion is given by the nonlinear tensor:

$$\widehat{\sigma}_{mesh} = \hat{J}^{-1}\alpha_u\hat{\nabla}\hat{u}_f,$$

where $\hat{J}^{-1}\alpha_u > 0$ is used to control the fluid mesh motion. The Neumann coupling conditions on $\widehat{\Gamma}_i$ are fulfilled in a variational way and cancel in monolithic modeling due to the global test space \hat{V}^0 in which the test functions from both the fluid and the solid subdomains coincide on the interface. Thus, the condition

$$\langle \hat{J}\hat{\sigma}_f\hat{F}^{-T}\hat{n}_f, \hat{\psi}^v \rangle_{\widehat{\Gamma}_i} + \langle [\hat{F}\hat{\Sigma} + \hat{\Sigma}_v(\hat{v})]\hat{n}_s, \hat{\psi}^v \rangle_{\widehat{\Gamma}_i} = 0 \quad \forall \hat{\psi}^v \in \hat{V}^0 \quad (13)$$

is implicitly contained in the above system.

2.6. Variational phase-field for dynamic pressurized-fractures

The phase-field fracture model will be composed of the dynamic model presented in [52, 51], the thermodynamically-consistent approach of [59], and the pressurized crack model of [61]. In extension to the previous section, we consider now a fracture C (with boundary ∂C) that is located in the solid Ω_s . In phase-field-based fracture propagation, the unknown solution variables are displacements $u_s : \Omega_s \cup \overline{C} \rightarrow \mathbb{R}^2$ and a smoothed indicator phase-field function $\varphi : \Omega_s \cup \overline{C} \rightarrow [0, 1]$. Here $\varphi = 0$ denotes the crack region and $\varphi = 1$ characterizes the unbroken material. The intermediate values $0 < \varphi < 1$ constitute a smooth transition zone dependent on a regularization parameter ε . The physics of the underlying problem ask to enforce a crack irreversibility condition (the crack can never heal) that is an inequality condition in time:

$$\partial_t \varphi \leq 0. \quad (14)$$

Consequently, modeling of fracture evolution problems leads to a variational inequality system, that is always, due to this constraint, quasi-stationary or time-dependent.

2.6.1. The dynamic phase-field fracture model (without internal pressure)

In this section, we first state the phase-field inequality in the strong form. The corresponding solid part has already been provided in Section 2.4.1. In particular, the strong form of the phase-field part reads: Find $\varphi : \Omega_s \cup \bar{C} \rightarrow [0, 1]$ such that

$$\begin{aligned} (1 - \kappa)(\Sigma(u_s) + \Sigma_v(v_s)) : E_{lin}(u_s)\varphi - G_c \varepsilon \Delta \varphi - \frac{G_c}{\varepsilon}(1 - \varphi) &\leq 0, \quad \partial_t \varphi \leq 0 \quad \text{in } \Omega_s \cup C, \\ \left[(1 - \kappa)(\Sigma(u_s) + \Sigma_v(v_s)) : E_{lin}(u_s)\varphi - G_c \varepsilon \Delta \varphi - \frac{G_c}{\varepsilon}(1 - \varphi) \right] \cdot \partial_t \varphi &= 0 \quad \text{in } \Omega_s \cup C, \\ \partial_n \varphi &= 0 \quad \text{on } \Gamma_D \cup \Gamma_i, \\ \varphi(0) &= 1 \text{ in } \Omega_s \times \{0\}, \quad \varphi(0) = 0 \text{ in } C \times \{0\}. \end{aligned}$$

Here, κ is a positive regularization parameter for the elastic energy, with $\kappa = o(\varepsilon)$ [3, 14] and G_c is the critical energy release rate.

The variational Euler-Lagrange system for dynamic fracture including an elastic dissipation term (similar to [52, 51]) reads:

Formulation 4. Setting $E(\varphi) = (1 - \kappa)\varphi^2 + \kappa$, we find $\{u_s, \varphi\} \in V_s^0 \times W$ for almost all times $t \in I$ such that

$$(\rho_s \partial_t^2 u_s, \psi_s^u) + (E(\varphi) \Sigma(u_s), \nabla \psi_s^u) + (E(\varphi) \Sigma_v(v_s), \nabla \psi_s^u) - \langle E(\varphi)[\Sigma(u_s) + \Sigma_v(v_s)] n_s, \psi_s^u \rangle_{\Gamma_i \cup \partial C} = 0 \quad \forall \psi_s^u \in V_s^0, \quad (15)$$

$$\begin{aligned} (1 - \kappa)(\varphi (\Sigma(u_s) + \Sigma_v(v_s)) : E_{lin}(u_s), \psi_s^\varphi - \varphi) \\ + G_c \left(-\frac{1}{\varepsilon}(1 - \varphi, \psi_s^\varphi - \varphi) + \varepsilon(\nabla \varphi, \nabla(\psi_s^\varphi - \varphi)) \right) \geq 0 \quad \forall \psi_s^\varphi \in W \cap L^\infty(\Omega_s \cup C). \end{aligned} \quad (16)$$

2.6.2. Interface coupling conditions for pressurized fractures

In the presence of pressurized fractures, a nonhomogeneous Neumann condition is applied to the crack surface; a detailed derivation for quasi-static brittle fracture and corresponding mathematical analysis can be found in [61, 62]. We assume that $\varepsilon > 0$ such that the crack is a thin and a priori empty object (i.e., width much smaller than its length) in the same dimension as the other equations; see Figure 2.

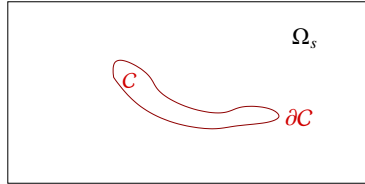


Figure 2: A crack C with boundary ∂C embedded in a solid Ω_s .

The pressure that acts on the surface ∂C of the fracture C is included via an interface law that corresponds to the dynamic coupling law of the FSI interface; namely continuity of normal tractions. Following the ideas of [61], we assume that the leading order of the fracture pressure is $-p_F I$. Since however the fracture interface is smeared out in the zone $0 < \varphi < 1$, a straightforward application of the dynamic coupling condition cannot be realized; in particular for numerical computations. Thus the fracture pressure p_F on ∂C will be transformed into a domain integral using Gauss' divergence theorem.

The derivation is performed in Eulerian coordinates since the corresponding equations are formulated therein in this section. The normal stress interface condition reads in strong form:

$$E(\varphi)[\Sigma n_s + \Sigma_v(v_s)n_s] = -p_F n_s \quad \text{on } \partial C.$$

Inserting this condition into the solid boundary term in Equation (15) on the boundary part ∂C yields

$$\begin{aligned} -\langle E(\varphi)[\Sigma(u_s) + \Sigma_v(v_s)] n_s, \psi_s^u \rangle_{\partial C} &= \langle p_F n_s, \psi_s^u \rangle_{\partial C} = \int_{\Omega_s} \nabla \cdot (p_F \psi_s^u) dx - \int_{\Gamma_i} p_F n_s \cdot \psi_s^u ds \\ &= \int_{\Omega_s} p_F \nabla \cdot \psi_s^u dx + \int_{\Omega_s} \nabla p_F \psi_s^u dx - \int_{\Gamma_i} p_F n_s \cdot \psi_s^u ds. \end{aligned}$$

If we assume a piece-wise constant pressure $\nabla p_F \equiv 0$, then we arrive at

$$-\langle E(\varphi)[\Sigma(u_s) + \Sigma_v(v_s)] n_s, \psi_s^u \rangle_{\partial C} = \int_{\Omega_s} p_F \nabla \cdot \psi_s^u dx - \int_{\Gamma_i} p_F n_s \cdot \psi_s^u ds. \quad (17)$$

Following [61], we introduce the phase-field version of the right hand side in (17):

$$\int_{\Omega_s} p_F \nabla \cdot \psi_s^u dx - \int_{\Gamma_i} p_F n_s \psi_s^u ds \rightarrow \int_{\Omega_s} \varphi^2 p_F \nabla \cdot \psi_s^u dx - \int_{\Gamma_i} \varphi^2 p_F n_s \cdot \psi_s^u ds. \quad (18)$$

We notice that $E(\varphi) \approx \varphi^2$ since $\kappa = 10^{-10}$. The corresponding terms on the energy level read:

$$\int_{\Omega_s} \varphi^2 p_F \nabla \cdot u_s dx - \int_{\Gamma_i} \varphi^2 p_F n_s \cdot u_s ds. \quad (19)$$

It is trivial to see that differentiation of (19) with respect to u yields (18). However since φ is now present in (19), we also need to differentiate with respect to φ from which we obtain:

$$2 \int_{\Omega_s} \varphi p_F \nabla \cdot u_s \cdot \psi_s^\varphi dx - 2 \int_{\Gamma_i} \varphi p_F n_s \cdot u_s \psi_s^\varphi ds, \quad (20)$$

which must be added to Equation (16).

Remark 2.3 (Modification of the dynamic FSI coupling condition). Due to the developments in this section and the resulting interface term in Equation (18), the continuity of normal tractions on the FSI-interface; namely (11), must be updated to:

$$\hat{J}\hat{\sigma}_f \hat{F}^{-T} \hat{n}_f + E(\hat{\varphi})[\hat{F} \hat{\Sigma} \hat{n}_s + \hat{\Sigma}_v(\hat{v}) \hat{n}_s - \hat{J} \hat{p}_F \hat{F}^{-T} \hat{n}_s] = 0 \quad \text{on } \hat{\Gamma}_i, \quad (21)$$

where $\hat{J} \hat{p}_F \hat{F}^{-T} \hat{n}_s$ is the Lagrangian form of $p_F n_s$ using Nanson's formula.

Remark 2.4 (Multiple fractures). The previous derivations have been undertaken while tacitly assuming a single fracture with a constant p_F . However, the same derivation holds for multiple fractures with non-constant p_F . In that case, ∂C represents the set of all fracture boundaries and Gauss' divergence theorem can be applied accordingly. The crucial difficulty is the treatment of different p_F for different fractures. One possibility that has been proposed for pressurized fractures in poro-elasticity (which in particular holds true for elasticity) are weighted interpolations [60, 53].

2.6.3. A phase-field model for pressurized dynamic fractures

Combining the previous two subsections yields the following system:

Formulation 5. Let $p_F \in H^1(\Omega_s \cup C)$ be given. Find $\{u_s, \varphi\} \in V_s^0 \times W$ for almost all times $t \in I$ such that

$$\begin{aligned} &(\rho_s \partial_t^2 u_s, \psi_s^u) + (E(\varphi) \Sigma(u_s), \nabla \psi_s^u) + (E(\varphi) \Sigma_v(v_s), \nabla \psi_s^u) - \langle E(\varphi)[\Sigma(u_s) + \Sigma_v(v_s) - p_F] n_s, \psi_s^u \rangle_{\Gamma_i} \\ &\quad + (\varphi^2 p_F, \nabla \cdot \psi_s^u) = 0 \quad \forall \psi_s^u \in V_s^0, \\ &(1 - \kappa)(\varphi (\Sigma(u_s) + \Sigma_v(v_s)) : E_{lin}(u_s), \psi_s^\varphi - \varphi) + 2(\varphi p_F \nabla \cdot u_s, \psi_s^\varphi - \varphi) - \langle 2\varphi p_F n_s u_s, \psi_s^\varphi - \varphi \rangle_{\Gamma_i} \\ &\quad + G_c \left(-\frac{1}{\varepsilon} (1 - \varphi, \psi_s^\varphi - \varphi) + \varepsilon (\nabla \varphi, \nabla (\psi_s^\varphi - \varphi)) \right) \geq 0 \quad \forall \psi_s^\varphi \in W \cap L^\infty(\Omega_s \cup C). \end{aligned}$$

2.7. A first-order system of pressurized dynamic phase-field fracture in Lagrangian coordinates

We first split the second-order in time elastodynamics equation into a first order system as already performed in Formulation 2. This step allows us later to employ a One-step- θ time-stepping scheme. In a second stage, we transform the phase-field equation into Lagrangian coordinates; namely the equations are transformed with the help of \widehat{T} from $\widehat{\Omega}_s$ to Ω_s . The solid mapping is standard [20] and defined as the ALE mapping; but this time within the solid domain. All kinematic quantities such as the deformation gradient $\widehat{F} = I + \widehat{\nabla} \widehat{u}_s$ and its determinant \widehat{J} are defined correspondingly.

Formulation 6. Let $\widehat{p}_F \in H^1(\widehat{\Omega}_s \cup \widehat{C})$ be given. Find $\{\widehat{v}_s, \widehat{u}_s, \widehat{\varphi}\} \in \widehat{L}_s \times \widehat{V}_s^0 \times \widehat{W}$ for almost all times $t \in I$ such that

$$\begin{aligned} & (\widehat{\rho}_s \partial_t \widehat{v}_s, \widehat{\psi}_s^\nu) + (E(\widehat{\varphi}) \widehat{\Sigma}(\widehat{u}_s), \widehat{\nabla} \widehat{\psi}_s^\nu) + (E(\widehat{\varphi}) \widehat{\Sigma}_v(\widehat{v}_s), \widehat{\nabla} \widehat{\psi}^u) - \langle E(\widehat{\varphi}) [\widehat{\Sigma}(\widehat{u}_s) + \widehat{\Sigma}_v(\widehat{v}) - \widehat{J} \widehat{p}_F \widehat{F}^{-T}] \widehat{n}_s, \widehat{\psi}^u \rangle_{\widehat{\Gamma}_i} \\ & + (\widehat{\varphi}^2 \widehat{p}_F, \widehat{\nabla} \cdot (\widehat{J} \widehat{F}^{-1} \widehat{\psi}_s^\nu)) = 0 \quad \forall \widehat{\psi}_s^\nu \in \widehat{V}_s^0, \\ & \widehat{\rho}_s (\partial_t \widehat{u}_s - \widehat{v}_s, \widehat{\psi}_s^u) = 0 \quad \forall \widehat{\psi}_s^u \in \widehat{L}_s, \\ & (1 - \kappa) (\widehat{J} \widehat{\varphi} (\widehat{\Sigma} + \widehat{\Sigma}_v) : \widehat{E}, \widehat{\psi}_s^\varphi - \widehat{\varphi})_{\widehat{\Omega}_s} + 2 (\widehat{\varphi} \widehat{p}_F \widehat{\nabla} \cdot (\widehat{J} \widehat{F}^{-1} \widehat{u}_s), \widehat{\psi}_s^\varphi - \widehat{\varphi})_{\widehat{\Omega}_s} - \langle 2 \widehat{J} \widehat{\varphi} \widehat{p}_F \widehat{F}^{-T} \widehat{n}_s \widehat{u}_s, \widehat{\psi}_s^\varphi - \widehat{\varphi} \rangle_{\widehat{\Gamma}_i} \\ & + G_c \left(-\frac{1}{\varepsilon} (\widehat{J}(1 - \widehat{\varphi}), \widehat{\psi}_s^\varphi - \widehat{\varphi}) + \varepsilon (\widehat{J} (\widehat{\nabla} \widehat{\varphi} \widehat{F}^{-1}) \widehat{F}^{-T}, \widehat{\nabla} \widehat{\psi}_s^\varphi - \widehat{\nabla} \widehat{\varphi}) \right) \geq 0 \quad \forall \widehat{\psi}_s^\varphi \in \widehat{W} \cap L^\infty(\widehat{\Omega}_s \cup \widehat{C}). \end{aligned}$$

3. An augmented Lagrangian formulation of the coupled fluid-structure phase-field model

In this section, we time-discretize the crack irreversibility constraint (14) in order to formulate the variational inequality system as a penalized variational equation. All other time derivatives are treated later in Section 4. We first focus on the phase-field fracture model itself and formulate afterwards our final coupled FSI phase-field fracture framework.

3.1. Augmented Lagrangian formulation of the dynamic pressurized phase-field fracture model

We first address an augmented Lagrangian penalization for a fully-coupled phase-field fracture framework. This is in contrast to [73] in which the displacement phase-field system has been solved in a partitioned fashion. Such a technique has been employed due to the fact that the underlying energy functional is non-convex in both variables simultaneously [12, 10, 18] (see also a detailed discussion in [1]), which causes serious challenges in the numerical solution. Recently, a fully monolithic solution algorithm for quasi-static fracture has been proposed in [38]. Another robust (but heuristic) approach has been proposed in [43] where the phase-field variable has been time-lagged through extrapolation in the displacement equation. On the other hand, it seems that the non-convexity plays a less important role for dynamic phase-field fracture because, for instance, the authors of [9] were able to apply a monolithic solver for the coupled displacement-phase-field system. Second, from our own numerical experiences within the present paper, the monolithic scheme for elastodynamic fracture has been more robust and more accurate than the extrapolated scheme proposed in [43]. In fact, in terms of accuracy, several comparisons for both models (quasi-monolithic and fully monolithic) have been carried out for quasi-static brittle fracture in [78], which support our observations in the present paper.

We apply the augmented Lagrangian technique to relax the variational inequality in terms of a variational equality. First, we apply backward different time discretization to $\partial_t \varphi \leq 0$ in order to obtain an incremental version of the inequality constraint, first in Eulerian coordinates, and then in the transformed coordinate system:

$$\partial_t \varphi \leq 0 \quad \Rightarrow \frac{\varphi - \varphi^{old}}{k} \leq 0 \quad \Rightarrow \varphi \leq \varphi^{old} \quad \Rightarrow \widehat{\varphi} \leq \widehat{\varphi}^{old}, \quad (22)$$

here $\widehat{\varphi}^{old}$ represents later the previous time step solution, i.e., $\widehat{\varphi}^{old} := \widehat{\varphi}^{n-1}$. Furthermore, k denotes the time step size, but which does not play a role in this section. Following [34, 40] and our previous work [73], we obtain as augmented Lagrangian penalization:

$$\left[\Xi + \gamma (\widehat{\varphi} - \widehat{\varphi}^{old}) \right]^+, \quad (23)$$

where $\Xi \in L^2$ and $\gamma > 0$. Moreover, $[x]^+ := \max(x, 0)$. The key idea is to iterate the function Ξ in order to realize a reliable approximation to the constraint.

Remark 3.1. The temporal inequality constraint (22) does also allow for an ALE formulation when starting on the time-continuous level while employing the ALE transformation and ALE time-derivative:

$$\partial_t \varphi \leq 0 \quad \text{in } \Omega \quad \Rightarrow \quad \hat{J} \partial_t \hat{\varphi} - \hat{J} \hat{F}^{-1} \hat{w} \cdot \hat{\nabla} \hat{\varphi} \leq 0 \quad \text{in } \hat{\Omega}.$$

Inserting the penalization term (23) into Formulation 6 replaces the variational inequality system by a penalized variational equality:

Formulation 7 (Monolithic augmented Lagrangian phase-field fracture in $\hat{\Omega}_s$). Given \hat{p}_F and Ξ . Find $\{\hat{v}_s, \hat{u}_s, \hat{\varphi}\} \in \hat{L}_s \times \hat{V}_s^0 \times \hat{W}$ for almost all times $t \in I$ such that

$$\begin{aligned} & (\hat{\rho}_s \partial_t \hat{v}_s, \hat{\psi}_s^\nu)_{\hat{\Omega}_s} + (E(\hat{\varphi}) \hat{F} \hat{\Sigma}, \hat{\nabla} \hat{\psi}_s^\nu)_{\hat{\Omega}_s} + (E(\hat{\varphi}) \hat{\Sigma}_v, \hat{\nabla} \hat{\psi}_s^\nu)_{\hat{\Omega}_s} - \langle E(\hat{\varphi}) [\hat{\Sigma}(\hat{u}_s) + \hat{\Sigma}_v(\hat{v}_s) - \hat{J} \hat{p}_F \hat{F}^{-T}] \hat{n}_s, \hat{\psi}_s^\nu \rangle_{\hat{\Gamma}_i} \\ & + (\hat{\varphi}_s^2 \hat{p}_F, \hat{\nabla} \cdot (\hat{J} \hat{F}^{-1} \hat{\psi}_s^\nu)) = 0 \quad \forall \hat{\psi}_s^\nu \in \hat{V}_s^0, \\ & \hat{\rho}_s (\partial_t \hat{u}_s - \hat{v}_s, \hat{\psi}_s^\mu)_{\hat{\Omega}_s} = 0 \quad \forall \hat{\psi}_s^\mu \in \hat{L}_s, \\ & (1 - \kappa) (\hat{J} \hat{\varphi} (\hat{\Sigma} + \hat{\Sigma}_v) : \hat{E}, \hat{\psi}_s^\varphi)_{\hat{\Omega}_s} + 2 (\hat{\varphi} \hat{p}_F \hat{\nabla} \cdot (\hat{J} \hat{F}^{-1} \hat{u}_s), \hat{\psi}_s^\varphi)_{\hat{\Omega}_s} - \langle 2 \hat{J} \hat{\varphi} \hat{p}_F \hat{F}^{-T} \hat{n}_s \hat{u}_s, \hat{\psi}_s^\varphi \rangle_{\hat{\Gamma}_i} \\ & + G_c \left(-\frac{1}{\varepsilon} (\hat{J}(1 - \hat{\varphi}), \hat{\psi}_s^\varphi) + \varepsilon (\hat{J} (\hat{\nabla} \hat{\varphi} \hat{F}^{-1}) \hat{F}^{-T}, \hat{\nabla} \hat{\psi}_s^\varphi) \right)_{\hat{\Omega}_s} \\ & + \left(\hat{J} [\Xi + \gamma(\hat{\varphi} - \hat{\varphi}^{old})]^+, \hat{\psi}_s^\varphi \right)_{\hat{\Omega}_s} = 0 \quad \forall \hat{\psi}_s^\varphi \in H^1(\hat{\Omega}_s \cup \hat{C}). \end{aligned}$$

3.2. The final system: coupling fluid-structure with phase-field fracture

We combine Formulation 3 and Formulation 7 and obtain the final system:

Formulation 8 (A variational-monolithic ALE-FSI phase-field fracture framework in $\hat{\Omega}$). Let $\hat{p}_F \in H^1(\hat{\Omega}_s \cup \hat{C})$ be given. Find a global vector-valued velocity, vector-valued displacements, a scalar-valued fluid pressure, and a scalar-valued phase-field function, that is to say that $\{\hat{v}, \hat{u}_f, \hat{u}_s, \hat{p}_f, \hat{\varphi}\} \in \{\hat{v}^D + \hat{V}^0\} \times \{\hat{u}_f^D + \hat{V}_{f,\hat{u}}^0\} \times \hat{V}_s^0 \times \hat{L}_f^0 \times H^1(\hat{\Omega}_s \cup \hat{C})$, such that $\hat{v}(0) = \hat{v}^0$, $\hat{u}_f(0) = \hat{u}_f^0$, $\hat{u}_s(0) = \hat{u}_s^0$ and $\hat{\varphi}(0) = \hat{\varphi}^0$ are satisfied, and for almost all times $t \in I$ holds:

$$\begin{aligned} \text{Fluid/solid momentum} & \left\{ \begin{aligned} & ((\hat{J} \hat{\rho}_f \partial_t \hat{v}, \hat{\psi}^\nu)_{\hat{\Omega}_f} + (\hat{\rho}_f \hat{J} (\hat{F}^{-1} (\hat{v} - \hat{w}) \cdot \hat{\nabla}) \hat{v}, \hat{\psi}^\nu)_{\hat{\Omega}_f} + (\hat{J} \hat{\sigma}_f \hat{F}^{-T}, \hat{\nabla} \hat{\psi}^\nu)_{\hat{\Omega}_f} \\ & + \langle \rho_f v_f \hat{J} (\hat{F}^{-T} \hat{\nabla} \hat{v}^T \hat{n}_f) \hat{F}^{-T}, \hat{\psi}^\nu \rangle_{\hat{\Gamma}_{out}} \\ & + (\hat{\rho}_s \partial_t \hat{v}, \hat{\psi}^\nu)_{\hat{\Omega}_s} + (E(\hat{\varphi}) \hat{F} \hat{\Sigma}, \hat{\nabla} \hat{\psi}^\nu)_{\hat{\Omega}_s} + (E(\hat{\varphi}) \hat{\Sigma}_v(\hat{v}), \hat{\nabla} \hat{\psi}^\nu)_{\hat{\Omega}_s} \\ & + (\hat{\varphi}_s^2 \hat{p}_F, \hat{\nabla} \cdot (\hat{J} \hat{F}^{-1} \hat{\psi}^\nu)) = 0 \quad \forall \hat{\psi}^\nu \in \hat{V}^0, \end{aligned} \right. \\ \text{Fluid mesh motion} & \left\{ \langle \hat{\sigma}_{\text{mesh}}, \hat{\nabla} \hat{\psi}_f^u \rangle_{\hat{\Omega}_f} = 0 \quad \forall \hat{\psi}_f^u \in \hat{V}_{f,\hat{u},\hat{\Gamma}_i}^0, \right. \\ \text{Solid momentum, 2nd eq.} & \left\{ \hat{\rho}_s (\partial_t \hat{u}_s - \hat{v}|_{\hat{\Omega}_s}, \hat{\psi}_s^\mu)_{\hat{\Omega}_s} = 0 \quad \forall \hat{\psi}_s^\mu \in \hat{L}_s, \right. \\ \text{Fluid mass conservation} & \left\{ \langle \hat{\text{div}} (\hat{J} \hat{F}^{-1} \hat{v}), \hat{\psi}_f^p \rangle_{\hat{\Omega}_f} = 0 \quad \forall \hat{\psi}_f^p \in \hat{L}_f^0, \right. \\ \text{Phase-field} & \left\{ \begin{aligned} & (1 - \kappa) (\hat{J} \hat{\varphi} (\hat{\Sigma} + \hat{\Sigma}_v) : \hat{E}, \hat{\psi}_s^\varphi)_{\hat{\Omega}_s} + 2 (\hat{\varphi} \hat{p}_F \hat{\nabla} \cdot (\hat{J} \hat{F}^{-1} \hat{u}_s), \hat{\psi}_s^\varphi)_{\hat{\Omega}_s} - \langle 2 \hat{J} \hat{\varphi} \hat{p}_F \hat{F}^{-T} \hat{n}_s \hat{u}_s, \hat{\psi}_s^\varphi \rangle_{\hat{\Gamma}_i} \\ & + G_c \left(-\frac{1}{\varepsilon} (\hat{J}(1 - \hat{\varphi}), \hat{\psi}_s^\varphi) + \varepsilon (\hat{J} (\hat{\nabla} \hat{\varphi} \hat{F}^{-1}) \hat{F}^{-T}, \hat{\nabla} \hat{\psi}_s^\varphi) \right)_{\hat{\Omega}_s} \\ & + \left(\hat{J} [\Xi + \gamma(\hat{\varphi} - \hat{\varphi}^{old})]^+, \hat{\psi}_s^\varphi \right)_{\hat{\Omega}_s} = 0 \quad \forall \hat{\psi}_s^\varphi \in H^1(\hat{\Omega}_s \cup \hat{C}). \end{aligned} \right. \end{aligned}$$

Remark 3.2. As in Formulation 3, the Neumann coupling conditions on $\hat{\Gamma}_i$ are fulfilled in a variational way and cancel in monolithic modeling. Thus, the condition

$$\langle \hat{\sigma}_f \hat{F}^{-T} \hat{n}_f, \hat{\psi}^\nu \rangle_{\hat{\Gamma}_i} + \langle E(\hat{\varphi}) [\hat{F} \hat{\Sigma} + \hat{\Sigma}_v(\hat{v}) - \hat{J} \hat{p}_F \hat{F}^{-T}] \hat{n}_s, \hat{\psi}^\nu \rangle_{\hat{\Gamma}_i} = 0 \quad \forall \hat{\psi}^\nu \in \hat{V}^0 \quad (24)$$

is implicitly contained in the above system.

Remark 3.3 (A note on the relation of the fracture pressure \hat{p}_F and the Navier-Stokes pressure \hat{p}_f). We strongly emphasize that the given fracture pressure \hat{p}_F is not coupled to the Navier-Stokes pressure \hat{p}_f in this paper. Mathematical modeling is out of scope in this work since significant steps have to be undertaken: let the fracture reach the FSI-interface Γ_i . Then, the phase-transition from solid to fluid must be modeled. Next, appropriate interpolation must connect \hat{p}_F to \hat{p}_f in the transition zone. Moreover, the fracture pressure will not be equally distributed anymore, which requires to model Stokes or Navier-Stokes flow in the fracture in order to compute an accurate \hat{p}_F . However, this last point requires extensive mathematical and numerical developments, although a similar procedure that has been developed in [60, 61, 53] might be applicable. Therein, phase-field is used as an indicator function to distinguish the damaged zone from the unbroken material in order to couple Darcy flow in the fracture with Darcy flow in a surrounding porous medium.

Remark 3.4 (Solid damping). According to our numerical simulations carried out in Section 5, solid damping $(E(\hat{\varphi})\hat{\Sigma}_v(\hat{v}), \hat{\nabla}\hat{\psi}^v)$ is currently indispensable for pressurized propagating fractures in a dynamic setting in order to obtain convergence of the nonlinear solver. This observation is supported by the analysis and comments made in [52]. Therein the authors had no pressure though but had to work with (strong) solid damping in order to establish well-posedness. From a mathematical point of view, the elastic dissipation term (strong solid damping) improves the regularity of the solid velocity, e.g., [37] (therefore, it is reasonable to work with the space \hat{V}^0 in which both the fluid and solid velocities are H^1 regular functions). In terms of fluid-structure interaction, the damping term changes naturally the response of the solid; nonetheless all difficulties in mathematical and numerical modeling of the overall coupled problem still remain. Thus, the challenge (and purpose) of this paper is not affected by adding solid damping. In Section 5.2 various sensitivity studies for different μ_v, λ_v are undertaken. A future topic will be to investigate whether in coupled FSI-PFF, solid damping can be completely neglected.

4. Discretization and solution algorithms

The coupled FSI phase-field problem in Formulation 8 is first formulated in terms of a single semilinear form and then solved with the Rothe method: first time, then space; which provides the flexibility to vary the spatial discretization during the time-stepping process. Finally, the discrete nonlinear problem is solved with a modified (or error-oriented) Newton method, which allows for increase of the residual. This Newton solver works as inner loop within an augmented Lagrangian iteration for enforcing the inequality constraint.

4.1. Time-stepping

In the domain $\widehat{\Omega}$ and the time interval $I = [0, T]$, we consider Formulation 8. Our goal is to apply A-stable finite differences in time. Specifically, time discretization is based on a One-step- θ scheme as presented for the pure FSI problem, Formulation 3, in [74]. Computational stability of these schemes has been investigated in [69]. With regard to general phase-field models discretized with second-order time-stepping schemes we refer to [41].

In more detail, semi-discretization in time yields a sequence of generalized steady-state problems that are completed by appropriate boundary values at every time step. Let

$$I = \{0\} \cup I_1 \cup \dots \cup I_N$$

be a partition of the time interval I into half open subintervals $I_n := (t_{n-1}, t_n]$ of (time step) size $k := k_n := t_n - t_{n-1}$ with

$$0 = t_0 < \dots < t_N = T.$$

Time derivatives are discretized with a backward difference quotient such that

$$\partial_t \hat{\varphi} \approx \frac{\hat{\varphi} - \hat{\varphi}^{n-1}}{k}, \quad \partial_t \hat{u} \approx \frac{\hat{u} - \hat{u}^{n-1}}{k}, \quad \partial_t \hat{v} \approx \frac{\hat{v} - \hat{v}^{n-1}}{k},$$

where $\hat{\varphi} := \hat{\varphi}^n := \hat{\varphi}(t_n)$, $\hat{u} := \hat{u}^n := \hat{u}(t_n)$, $\hat{v} := \hat{v}^n := \hat{v}(t_n)$, $\hat{\varphi}^{n-1} := \hat{\varphi}(t_{n-1})$, $\hat{u}^{n-1} := \hat{u}(t_{n-1})$, $\hat{v}^{n-1} := \hat{v}(t_{n-1})$. Furthermore, the mesh velocity $\partial_t \hat{\mathcal{A}} = \hat{w}$ is numerically realized as $\hat{w} = k^{-1}(\hat{u}_f - \hat{u}_f^{n-1})$.

Formulation 9 (The time-discretized abstract problem). We aim to find $\hat{U}^n = \{\hat{v}^n, \hat{u}_f^n, \hat{u}_s^n, \hat{p}_f^n, \hat{\varphi}_s^n\} \in \widehat{X}_D^0$, where $\widehat{X}_D^0 := \{\hat{v}^D + \hat{V}^0\} \times \{\hat{u}_f^D + \hat{V}_{f,u}^0\} \times \hat{V}_s^0 \times \hat{L}_f^0 \times H^1(\widehat{\Omega}_s \cup \widehat{C})$ and $\widehat{X} = \hat{V}^0 \times \hat{V}_{f,\hat{u},\widehat{\Gamma}_i}^0 \times \hat{V}_s^0 \times \hat{L}_f^0 \times H^1(\widehat{\Omega}_s \cup \widehat{C})$, for all $n = 1, 2, \dots, N$ such that

$$\hat{A}(\hat{U}^n)(\hat{\Psi}) = 0 \quad \forall \hat{\Psi} \in \widehat{X}, \quad (25)$$

where the semi-linear form $\hat{A}(\cdot)(\cdot)$ is split into

$$\hat{A}(\hat{U}^n)(\hat{\Psi}) := \hat{A}_T(\hat{U}^{n,t})(\hat{\Psi}) + \hat{A}_I(\hat{U}^n)(\hat{\Psi}) + \hat{A}_E(\hat{U}^n)(\hat{\Psi}) + \hat{A}_P(\hat{U}^n)(\hat{\Psi}).$$

Details of this decomposition are provided in Definition 4.1.

Definition 4.1 (Arranging the semi-linear form $\hat{A}(\hat{U}^n)(\hat{\Psi})$ into groups). We formally split the semilinear form into four categories: time equation terms (including the time derivatives); implicit terms (such as the fluid incompressibility and also the phase-field equation); pressure terms; and finally all ‘standard’ terms (stress terms, fluid convection, and elastic dissipation). In detail we have the decomposition:

$$\begin{aligned} \hat{A}_T(\hat{U})(\hat{\Psi}) &= (\hat{J}\hat{\rho}_f \partial_t \hat{v}, \hat{\psi}^v)_{\widehat{\Omega}_f} - (\hat{\rho}_f \hat{J}(\hat{F}^{-1} \hat{w} \cdot \hat{\nabla}) \hat{v}, \hat{\psi}^v)_{\widehat{\Omega}_f} + (\hat{\rho}_s \partial_t \hat{v}, \hat{\psi}^v)_{\widehat{\Omega}_s} + (\hat{\rho}_s \partial_t \hat{u}_s, \hat{\psi}_s^u)_{\widehat{\Omega}_s}, \\ \hat{A}_I(\hat{U})(\hat{\Psi}) &= (\widehat{\sigma}_{mesh}, \widehat{\nabla} \hat{\psi}_f^u)_{\widehat{\Omega}_f} + (\widehat{\operatorname{div}}(\hat{J}\hat{F}^{-1} \hat{v}), \hat{\psi}_f^p)_{\widehat{\Omega}_f} \end{aligned} \quad (26)$$

$$\begin{aligned} &+ (1 - \kappa)(\hat{J}\hat{\varphi}(\widehat{\Sigma} + \widehat{\Sigma}_v) : \hat{E}, \hat{\psi}_s^\varphi)_{\widehat{\Omega}_s} + 2(\hat{\varphi}\hat{p}_F \hat{\nabla} \cdot (\hat{J}\hat{F}^{-1} \hat{u}_s), \hat{\psi}_s^\varphi)_{\widehat{\Omega}_s} - \langle 2\hat{J}\hat{\varphi}\hat{p}_F \hat{F}^{-T} \hat{n}_s \hat{u}_s, \hat{\psi}_s^\varphi \rangle_{\widehat{\Gamma}_i} \\ &+ G_c \left(-\frac{1}{\varepsilon} (\hat{J}(1 - \hat{\varphi}), \hat{\psi}_s^\varphi) + \varepsilon (\hat{J}(\widehat{\nabla} \hat{\varphi} \hat{F}^{-1}) \hat{F}^{-T}, \widehat{\nabla} \hat{\psi}_s^\varphi) \right)_{\widehat{\Omega}_s} + \left(\hat{J}[\Xi + \gamma(\hat{\varphi} - \hat{\varphi}^{n-1})]^+, \hat{\psi}_s^\varphi \right)_{\widehat{\Omega}_s}, \end{aligned} \quad (27)$$

$$\begin{aligned} \hat{A}_P(\hat{U})(\hat{\Psi}) &= (\hat{J}\widehat{\sigma}_{f,p} \hat{F}^{-T}, \widehat{\nabla} \hat{\psi}^v)_{\widehat{\Omega}_f}, \\ \hat{A}_E(\hat{U})(\hat{\Psi}) &= (\hat{\rho}_f \hat{J}(\hat{F}^{-1} \hat{v} \cdot \hat{\nabla}) \hat{v}, \hat{\psi}^v)_{\widehat{\Omega}_f} + (\hat{J}\widehat{\sigma}_{f,vu} \hat{F}^{-T}, \widehat{\nabla} \hat{\psi}^v)_{\widehat{\Omega}_f} + \langle \rho_f v \hat{J}(\hat{F}^{-T} \widehat{\nabla} v_f^T) \hat{F}^{-T} \hat{n}, \hat{\psi}^v \rangle_{\widehat{\Gamma}_{out}} \\ &+ (E(\hat{\varphi}) \hat{F} \widehat{\Sigma}, \widehat{\nabla} \hat{\psi}^v)_{\widehat{\Omega}_s} + (E(\hat{\varphi}) \widehat{\Sigma}_v(\hat{v}), \widehat{\nabla} \hat{\psi}^v)_{\widehat{\Omega}_s} + (\hat{\varphi}_s^2 \hat{p}_F, \hat{\nabla} \cdot (\hat{J}\hat{F}^{-1} \hat{\psi}^v))_{\widehat{\Omega}_s} - (\hat{\rho}_s \hat{v}, \hat{\psi}_s^u)_{\widehat{\Omega}_s}, \end{aligned} \quad (28)$$

where the fluid stress tensor $\widehat{\sigma}_f$ is further split into $\widehat{\sigma}_{f,vu}$, $\widehat{\sigma}_{f,p}$:

$$\widehat{\sigma}_{f,p} = -\hat{p}_f \hat{I}, \quad \widehat{\sigma}_{f,vu} = \rho_f v \hat{J}(\widehat{\nabla} \hat{v} \hat{F}^{-1} + \hat{F}^{-T} \widehat{\nabla} \hat{v}^T).$$

The (nonlinear) time derivative in $\hat{A}_T(\hat{U})(\hat{\Psi})$ is approximated by a backward difference quotient. For the time step $t_n \in I$, for $n = 1, 2, \dots, N$ ($N \in \mathbb{R}$), we compute $\hat{v} := \hat{v}^n$, $\hat{u}_i := \hat{u}_i^n$ ($i = f, s$) via

$$\begin{aligned} \hat{A}_T(\hat{U}^{n,t})(\hat{\Psi}) &\approx \frac{1}{k} \left(\hat{\rho}_f \hat{J}^{n,\theta} (\hat{v} - \hat{v}^{n-1}), \hat{\psi}^v \right)_{\widehat{\Omega}_f} - \frac{1}{k} \left(\hat{\rho}_f (\hat{J}\hat{F}^{-1}(\hat{u}_f - \hat{u}_f^{n-1}) \cdot \hat{\nabla}) \hat{v}, \hat{\psi}^v \right)_{\widehat{\Omega}_f} \\ &+ \frac{1}{k} \left(\hat{\rho}_s (\hat{v} - \hat{v}^{n-1}), \hat{\psi}^v \right)_{\widehat{\Omega}_s} + \left(\hat{u}_s - \hat{u}_s^{n-1}, \hat{\psi}_s^u \right)_{\widehat{\Omega}_s}, \end{aligned} \quad (29)$$

where we introduce the parameter $\theta \in [0, 1]$. Furthermore, we use

$$\hat{J}^{n,\theta} = \theta \hat{J}^n + (1 - \theta) \hat{J}^{n-1},$$

and $\hat{u}_i^n := \hat{u}_i(t_n)$, $\hat{v}^n := \hat{v}(t_n)$, and $\hat{J} := \hat{J}^n := \hat{J}(t_n)$. The former time step is given by \hat{v}^{n-1} , etc. for $i = f, s$.

Formulation 10. Let the previous time step solution $\hat{U}^{n-1} = \{\hat{v}^{n-1}, \hat{u}_f^{n-1}, \hat{u}_s^{n-1}, \hat{p}_f^{n-1}, \hat{\varphi}_s^{n-1}\}$ and the time step $k := k_n = t_n - t_{n-1}$ be given. In order to solve (25), we seek $\hat{U}^n = \{\hat{v}^n, \hat{u}_f^n, \hat{u}_s^n, \hat{p}_f^n, \hat{\varphi}_s^n\} \in \widehat{X}^0$ by employing One-step-θ splitting:

$$\hat{A}_T(\hat{U}^{n,t})(\hat{\Psi}) + \theta \hat{A}_E(\hat{U}^n)(\hat{\Psi}) + \hat{A}_P(\hat{U}^n)(\hat{\Psi}) + \hat{A}_I(\hat{U}^n)(\hat{\Psi}) = -(1 - \theta) \hat{A}_E(\hat{U}^{n-1})(\hat{\Psi}). \quad (30)$$

The concrete scheme depends on the choice of the parameter $\theta \in [0, 1]$. For $\theta = 1$ we obtain the strongly A-stable backward Euler scheme (BE). For $\theta = 0.5 + k_{shift}$, we obtain the 2nd order (shown for linear parabolic problems in [65, 45]), A-stable, globally stabilized, Crank-Nicolson scheme (CNs), which is shifted in this paper by $k_{shift} = 0.01s$ towards the implicit side. Ideally, one could use $k_{shift} = k_n$, which however requires the computation of a characteristic time step size with $k_n \ll 0.5$ because the choice $k_{shift} = k_n \geq 0.5$ is useless since $\theta \geq 1$ would follow.

Remark 4.1. Formulation 10 is still nonlinear and continuous on the spatial level.

4.2. Spatial discretization

The time discretized Formulation 10 is the starting point for the Galerkin discretization in space. To this end, we construct finite dimensional subspaces $\widehat{X}_h^0 \subset \widehat{X}^0$ to find an approximate solution to the continuous problem. As previously explained, in the context of our variational-monolithic formulation, the computations are done on the reference configuration $\widehat{\Omega}$. We use two dimensional shape-regular meshes. A mesh consists of quadrilateral cells \hat{K} . They perform a non-overlapping cover of the computation domain $\widehat{\Omega} \subset \mathbb{R}^d$, $d = 2, 3$. The corresponding mesh is given by $\hat{\mathcal{T}}_h = \{\hat{K}\}$. The discretization parameter in the reference configuration is denoted by \hat{h} and is a cell-wise constant that is given by the diameter $\hat{h}_{\hat{K}}$ of the cell \hat{K} .

On $\hat{\mathcal{T}}_h$, the conforming finite element space for $\{\hat{v}_h, \hat{u}_{f,h}, \hat{u}_{s,h}, \hat{p}_{f,h}, \hat{\varphi}_{s,h}\}$ is denoted by the space $\widehat{X}_h \subset \widehat{X}$. For Navier-Stokes flow, we prefer the biquadratic, discontinuous-linear Q_2^c/P_1^{dc} element. The definitions of the spaces for the velocities, displacements, pressure, and phase-field unknowns on a time interval I_m read:

$$\begin{aligned}\hat{V}_h &:= \{\hat{v}_h \in [C(\hat{\Omega}_h)]^d, \hat{v}_h|_{\hat{K}} \in [Q_2^c(\hat{K})]^d \quad \forall \hat{K} \in \hat{\mathcal{T}}_h, \hat{v}_h|_{\hat{\Gamma} \setminus \hat{\Gamma}_i} = 0\}, \\ \hat{U}_{f,h} &:= \{\hat{u}_h \in [C(\hat{\Omega}_h)]^d, \hat{u}_h|_{\hat{K}} \in [Q_2^c(\hat{K})]^d \quad \forall \hat{K} \in \hat{\mathcal{T}}_h, \hat{u}_h|_{\hat{\Gamma} \setminus \hat{\Gamma}_i} = 0\}, \\ \hat{U}_{s,h} &:= \{\hat{u}_h \in [C(\hat{\Omega}_h)]^d, \hat{u}_h|_{\hat{K}} \in [Q_2^c(\hat{K})]^d \quad \forall \hat{K} \in \hat{\mathcal{T}}_h, \hat{u}_h|_{\hat{\Gamma} \cup \hat{\Gamma}_i} = 0\}, \\ \hat{P}_{f,h} &:= \{\hat{p}_h \in [\hat{L}^2(\hat{\Omega}_h)], \hat{p}_h|_{\hat{K}} \in [P_1^{dc}(\hat{K})] \quad \forall \hat{K} \in \hat{\mathcal{T}}_h\}, \\ \hat{\Phi}_{s,h} &:= \{\hat{\varphi}_h \in [C(\hat{\Omega}_h)]^d, \hat{\varphi}_h|_{\hat{K}} \in [Q_1^c(\hat{K})]^d \quad \forall \hat{K} \in \hat{\mathcal{T}}_h, \hat{\varphi}_h|_{\hat{\Gamma} \setminus \hat{\Gamma}_i} = 0\}.\end{aligned}$$

We consider for each $\hat{K} \in \hat{\mathcal{T}}_h$ the bilinear transformation $\hat{\sigma}_K : \hat{K}_{\text{unit}} \rightarrow \hat{K}$, where \hat{K}_{unit} denotes the master cell. Then, the Q_1^c and Q_2^c elements are defined by

$$\begin{aligned}Q_1^c(\hat{K}) &= \{q \circ \hat{\sigma}_K^{-1} : q \in \text{span} < 1, x, y, xy >\}, \\ Q_2^c(\hat{K}) &= \{q \circ \hat{\sigma}_K^{-1} : q \in \text{span} < 1, x, y, xy, x^2, y^2, x^2y, y^2x, x^2y^2 >\}\end{aligned}$$

with $\dim Q_1^c = 4$ and $\dim Q_2^c = 9$. The P_1^{dc} element consists of linear functions defined by

$$P_1^{dc}(\hat{K}) = \{q \circ \hat{\sigma}_K^{-1} : q \in \text{span} < 1, x, y >\}$$

with $\dim P_1^{dc}(\hat{K}) = 3$.

The property of the Q_2^c/P_1^{dc} element is continuity of the velocity values across different mesh cells [39]. However, the pressure is defined by discontinuous test functions. Therefore, this element preserves local mass conservation, is of low order, gains the *inf-sup stability*, and is an optimal choice for both fluid problems and fluid-structure interaction problems.

Formulation 11. Let the previous, spatially discretized, time step solution $\hat{U}_h^{n-1} = \{\hat{v}_h^{n-1}, \hat{u}_{f,h}^{n-1}, \hat{u}_{s,h}^{n-1}, \hat{p}_{f,h}^{n-1}, \hat{\varphi}_{s,h}^{n-1}\}$ be given. We seek $\hat{U}_h^n = \{\hat{v}_h^n, \hat{u}_{f,h}^n, \hat{u}_{s,h}^n, \hat{p}_{f,h}^n, \hat{\varphi}_{s,h}^n\} \in \widehat{X}_h^0$ via

$$\hat{A}_T(\hat{U}_h^{n,t})(\hat{\Psi}_h) + \theta \hat{A}_E(\hat{U}_h^n)(\hat{\Psi}_h) + \hat{A}_P(\hat{U}_h^n)(\hat{\Psi}_h) + \hat{A}_I(\hat{U}_h^n)(\hat{\Psi}_h) = -(1 - \theta) \hat{A}_E(\hat{U}_h^{n-1})(\hat{\Psi}_h) \quad \forall \hat{\Psi} \in \widehat{X}_h. \quad (31)$$

4.3. Solution algorithms

At each time step t_n , we design as outer loop an augmented Lagrangian iteration (indexed by k in the following) in order to enforce the crack irreversibility constraint. At each augmented Lagrangian step, in the inner loop, the nonlinear, spatially discretized coupled forward Formulation 11 is solved with Newton's method. At each Newton iteration a linear equation system is solved.

4.3.1. Augmented Lagrangian iteration as outer loop

Per time step, we have to compute a penalization function Ξ for the irreversibility constraint. The key idea in the augmented Lagrangian method is to iterate in order to obtain the correct penalization. Thus, for the iteration steps $k = 1, 2, 3, \dots$ we have

$$\Xi_{h,k+1} = (\Xi_{h,k} + \gamma(\hat{\varphi}_{h,k+1} - \hat{\varphi}_h^{n-1}))_+, \quad k = 0, 1, 2, \dots$$

Algorithm 4.2 (Augmented Lagrangian loop). At t^0 let $\Xi_{h,0}$ be given, e.g., $\Xi_{h,0} = 0$. Moreover, let $\gamma > 0$ be fixed and given for all t_n . For $k = 0, 1, 2, \dots$

1. Given $\Xi_{h,k}$ and $\hat{\varphi}_h^{n-1}$; we seek $\hat{U}_{h,k+1}^n$ by solving Formulation 11 with Newton's method via Algorithm 4.3.
2. Update
$$\Xi_{h,k+1} = (\Xi_{h,k} + \gamma(\hat{\varphi}_{h,k+1} - \hat{\varphi}_h^{n-1}))_+$$
3. Check the stopping criterion
$$\|\Xi_{h,k+1} - \Xi_{h,k}\| \leq \text{TOL}_{\text{AL}}, \quad \text{TOL}_{\text{AL}} > 0.$$
4. Set: $\hat{U}_h^n := \hat{U}_{h,k^*}^n$ where k^* is the k which satisfies the stopping criterion.
5. Increment $t_n \rightarrow t_{n+1}$.

In this work we modify Algorithm 4.2 and iterate in the first time steps to obtain an appropriate Ξ . Then, we keep this Ξ for the remaining time steps and perform no longer augmented Lagrangian steps at each time step. This procedure significantly reduces the computational cost and still yields good satisfaction of the constraint.

4.3.2. Inner loop: Nonlinear iterations using Newton's method

For the nonlinear problem that arises in this paper, we cannot always expect a monotone decrease of Newton's residual. In particular, the monolithic formulation of the phase-field subproblem requires already a modification of Newton's method that allows for a temporary increase of the residuals [38]. Consequently, the coupled FSI-PFF problem inherits the bad characteristics of the phase-field subproblem.

To this end, temporal (indexed by n) and spatial (indexed by h) discretization results per augmented Lagrangian step (indexed by k) within each single time step in a nonlinear quasi-stationary problem

$$\hat{A}(\hat{U}_{h,k}^n)(\hat{\Psi}) = 0 \quad \forall \hat{\Psi} \in \hat{X}_h,$$

which is solved by Newton's method. Still, the semilinear form $\hat{A}(\cdot)(\cdot)$ is decomposed as explained in Formulation 10 or 11, respectively.

Algorithm 4.3. For fixed n, h, k , let an initial Newton guess $\hat{U}_{h,k}^{n,0}$ be given. Find for $j = 0, 1, 2, \dots$ the update $\delta\hat{U}_{h,k}^{n,j}$ of the linear defect-correction problem

$$\begin{aligned} \hat{A}'(\hat{U}_{h,k}^{n,j})(\delta\hat{U}_{h,k}^{n,j}, \hat{\Psi}) &= -\hat{A}(\hat{U}_{h,k}^{n,j})(\hat{\Psi}), \\ \hat{U}_{h,k}^{n,j+1} &= \hat{U}_{h,k}^{n,j} + \omega\delta\hat{U}_{h,k}^{n,j}. \end{aligned} \tag{32}$$

Here, $\omega \in (0, 1]$ is a damping parameter. Since phase-field fracture leads to an indefinite Jacobian matrix in a monolithic formulation, Newton's method with a classical residual-based convergence criterion, i.e.,

$$\|A(U_{h,k}^{n,j+1})(\Psi_h)\|_{l^2} < \|A(U_{h,k}^{n,j})(\Psi_h)\|_{l^2} \tag{33}$$

will not always work. Therefore, we rather employ an error-oriented version in which the stopping criterion is based on sufficient decrease of the updates, i.e.,

$$\|\delta\hat{U}_{h,k,simp}^{n,j+1}\|_{l^2} < \|\delta\hat{U}_{h,k}^{n,j}\|_{l^2},$$

where $\delta\hat{U}_{h,k,simp}^{n,j+1}$ is a simplified Newton update with new right hand side but old matrix; all details of this algorithm can be found in [24]. For quasi-static brittle phase-field fracture both residual-based and error-oriented Newton methods have been implemented and compared in [78].

Remark 4.2. As heuristic alternative, one can still work with a residual-based Newton algorithm with backtracking line search with $\omega := a^l$, e.g., $a = 0.6$. Then a (small) fixed number of line search steps, e.g., $l = 4$ is performed. Even if for the maximal $l = 4$, criterion (33) is violated, we accept $\|A(U_{h,k}^{n,j+1})(\Psi_h)\|_{l^2}$, and go to the next Newton step $j \rightarrow j+1$. As for the error-oriented Newton method, this procedure allows for a temporary increase of the residual and works fine in practice for the examples in this paper in which this feature is required. However, there is no theoretical justification that this approach always works.

The directional derivative (omitting all indices) $\hat{A}'(\hat{U})(\delta\hat{U}, \hat{\Psi})$ for the Jacobian is defined by

$$\hat{A}'(\hat{U})(\delta\hat{U}, \hat{\Psi}) := \lim_{\varepsilon \rightarrow 0} \frac{1}{\varepsilon} \left\{ \hat{A}(\hat{U} + \varepsilon\delta\hat{U})(\hat{\Psi}) - \hat{A}(\hat{U})(\hat{\Psi}) \right\} = \frac{d}{d\varepsilon} \left. \hat{A}_h(\hat{U} + \varepsilon\delta\hat{U})(\hat{\Psi}) \right|_{\varepsilon=0}.$$

As the residual, the Jacobian is split into four categories and is then evaluated analytically and most details are omitted for convenience of the reader. Here, we present one representative example:

$$\hat{A}_{mesh}(\hat{U})(\hat{\Psi}) := (\widehat{\sigma}_{mesh}, \widehat{\nabla}\hat{\psi}_f^u), \quad \sigma_{mesh} = \hat{J}^{-1} \alpha_u \widehat{\nabla}\hat{u}_f, \quad (34)$$

$$\rightarrow \hat{A}'_{mesh}(\hat{U})(\delta\hat{U}, \hat{\Psi}) := (-\hat{J}^{-2} \hat{J}'(\delta U) \alpha_u \widehat{\nabla}\hat{u}_f + \hat{J}^{-1} \alpha_u \widehat{\nabla}\delta\hat{u}_f, \widehat{\nabla}\hat{\psi}_f^u), \quad (35)$$

where $\hat{J}'(\delta\hat{U})$ denotes the directional derivative of \hat{J} with respect to \hat{u} . All details for pure variational-monolithic ALE-FSI in $\widehat{\Omega}$ can be found in [74, 76] with the respective programming code in [75].

Remark 4.3 (Quasi-Newton steps). In order to reduce computational cost, quasi-Newton steps are applied if the decrease of two subsequent Newton iterates is sufficiently good (here a factor of < 0.1). Then the Jacobian matrix from the previous step is kept and only the right hand side in (32) is updated.

Remark 4.4 (Dirichlet boundary conditions). In Newton's method, non-homogeneous Dirichlet boundary conditions are only prescribed on the initial guess $\hat{U}_{h,k}^{n,0}$ and in all further updates non-homogeneous Dirichlet conditions are replaced by homogeneous Dirichlet conditions.

Remark 4.5. At each Newton step, the linear equation systems are solved with the direct solver UMFPACK [23]. The main reason is that the development of robust linear iterative solvers and efficient preconditioners for the fully coupled Formulation 8 is extremely challenging and beyond the frame of this paper. Of course, alternatively, partitioned approaches can be developed such that efficient solvers for each subproblem can be employed. But also here, due to the coupling of so many different equations, careful development of robust and efficient methods, and the ordering of such a coupling will take significant effort and is hence also without the scope of this paper.

5. Numerical tests

The purpose of this section is to investigate the proposed framework with respect to computational stability and correctness of numerical modeling. In particular, we compute goal functionals on different spatial meshes and different time step sizes. In the first two Sections 5.1 and 5.2, the focus is more on fluid-structure interaction. Here the fracture is pressurized and not propagating, while on the other hand the FSI interaction yields moderate and large solid deformations. Specifically, in Section 5.2, sensitivity with respect to different solid damping parameters is addressed. In the third and fourth Sections 5.3 and 5.4, the solid deformations are rather small, but the pressure in the fracture exceeds a critical value causing the fracture(s) to grow in their length. In the last Section 5.5, two configurations with rather large solid deformations and evolving fractures are considered; in particular, the fracture(s) will interact with the FSI-interface. In all examples, the Reynolds numbers are such that we work in a laminar flow regime. The examples are computed with the finite element package deal.II [7, 6] by implementing the method from [73] in the open source FSI code [75].

5.1. Example 1: A fixed fracture, moderate flow, and moderate solid deformation

In this first example we consider a fixed (non-propagating) fracture in the solid part. The flow is moderate and first leads to an oscillating obstacle and finally results in a stationary flow profile. The aim of this first test are convergence tests in time and space for various goal functionals.

Configuration. The geometry and notation are provided in Figure 3. Here, the initial fracture is initialized by the initial condition $\hat{\varphi}^0 = 0$ in $\Omega_C := (0.875m, 0.9375m) \times (0.25m, 0.625m)$. Three mesh levels are obtained from 3, 4 and 5-times uniform refinement resulting in 2 048, 8 192 and 32 768 mesh cells (in the following labeled as Ref. 3, 4, 5, respectively). This corresponds to 41 829, 165 573 and 658 821 spatial degrees of freedom per linear solve and $h = 0.044m$, $0.022m$ and $h = 0.011m$. More specifically on the finest mesh level Ref. 5 we deal with 263682 degrees

of freedom for the velocity, 263682 degrees of freedom for the displacements, 98304 degrees of freedom for the pressure and 33153 degrees of freedom for the phase-field variable.

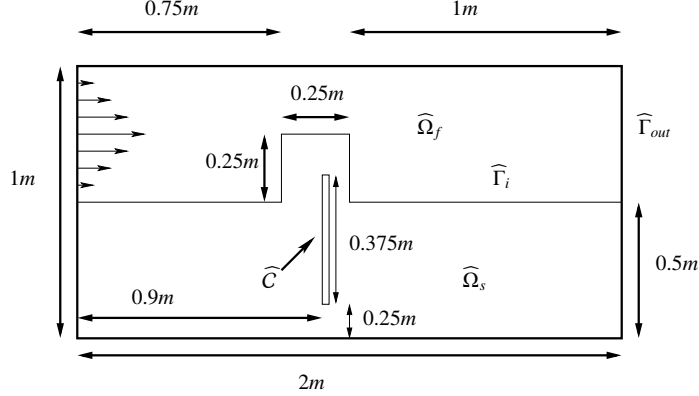


Figure 3: Notation and configuration of the Sections 5.1, 5.3 and 5.4.

Boundary and initial conditions. For the upper, lower, and left boundaries, ‘no-slip’ conditions for velocity and zero displacements for the solid are prescribed. At the fluid outlet $\hat{\Gamma}_{out}$, the ‘do-nothing’ outflow condition [46] is imposed. Moreover, $\hat{u} = 0$ on $\hat{\Gamma}_{out}$. For the phase-field variable $\hat{\varphi}$ ‘natural’ boundary conditions are of homogeneous Neumann type. However, on the left and right boundaries as well as on $\hat{\Gamma}_i$, we set $\hat{\varphi} = 1$ (no fracture) since at these boundaries where the FSI interface $\hat{\Gamma}_i$ joins, fractures might develop if not explicitly prevented; we refer the reader also to the Examples 5a/b.

A parabolic inflow velocity profile is given on $\hat{\Gamma}_{in}$ by

$$v_f(0, y) = \bar{U}(y - 1)(y - 0.5), \quad \bar{U} = 0.1 \text{ ms}^{-1}.$$

For $t < 2.0\text{s}$, $v_f(0, y)$ is scaled with $\frac{1-\cos(\frac{\pi}{2}t)}{2}$ in order to have a smooth inflow profile.

Parameters. For the fluid we use $\varrho_f = 1 \text{ kg m}^{-3}$, $\nu_f = 10^{-2} \text{ m}^2 \text{s}^{-1}$. The elastic solid is characterized by $\varrho_s = 10 \text{ kg m}^{-3}$, $\nu_s = 0.2$, $\mu_s = 1 \text{ kg m}^{-1} \text{s}^{-2}$. The fracture pressure is $\hat{p}_F = 10^{-2} \text{ Pa}$. The model parameter $\varepsilon = 0.044 = h_{coarse}$ is fixed in all computations as well as $\kappa = 10^{-10}$. Furthermore, $\gamma = 50$ and $G_c = 1 \text{ N/m}$. The (absolute) Newton tolerance is chosen as 10^{-8} . In the first time step, we determine an appropriate penalization parameter with the help of the augmented Lagrangian algorithm. In the remaining time steps, we keep this penalization parameter fixed. The time step size is $k = 1 \text{ s}$ and the total time $T = 50 \text{ s}$. As time stepping scheme, we use the shifted Crank–Nicolson scheme. The solid damping parameters are $\mu_v = \lambda_v = 0$ in this example.

The maximal velocity is $v_{max} = 0.012 \text{ m/s}$. The lowest channel width is $D = 0.25 \text{ m}$. Thus, the Reynolds number is $Re = \frac{v_{max}D}{\nu_f} = 0.3$, which is a rather small value. However, also the elasticity parameters are very small, too, and for this reason a moderate solid deformation is observed.

Quantities of interest. We compute various goal functionals that cover different parts of the model:

- Evaluation of $\hat{u}_x(1, 0.75)$ and $\hat{u}_y(1, 0.75)$ (related to solid modeling);
- Evaluation of stresses in x and y direction (drag and lift) on the FSI-interface $\hat{\Gamma}_i$, which are related to FSI modeling.

Discussion of our findings. The results to this first example are shown in the Figures 4 to 8. In Figure 4 the numerical solutions for the different variables $v_f, \varphi_s, p_f, \Xi, u_{f,s}$ in the deformed domain $\Omega = \Omega(T = 50\text{s})$ are visualized. In the remaining figures convergence tests in time and space for the above goal functionals are presented. To investigate temporal convergence, the mesh level is fixed at Ref. 4. For the spatial convergence test, we fix the time step size at $k = 0.5\text{s}$. Here, we clearly identify convergence in all goal functionals.

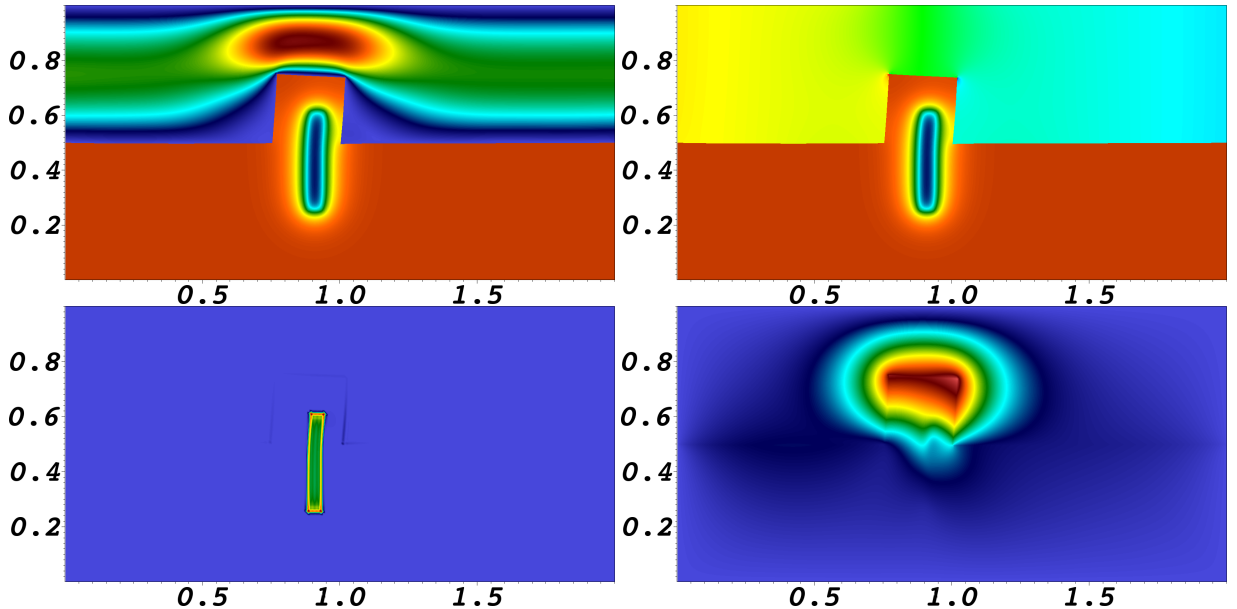


Figure 4: Example 1 at $T = 50\text{s}$. Going from top left to bottom right: First the flow field (with maximum velocity of 0.012m/s) and the fracture location are shown. The fracture is characterized by $\hat{\varphi} = 0$ (blue). Next, the pressure field is shown. The pressure is zero (blue) at the outflow boundary, which is due to the do-nothing condition and related normalization. The pressure has singularities at the two corners of the obstacle. In the third figure, the augmented Lagrangian penalization function Ξ is shown. The largest values of about 86.5 (in red color) are found on the fracture boundary $\partial\bar{C}$ and particularly in the four corners. Finally, the magnitude of the displacement field is shown. The maximum is about 0.023m (in red).

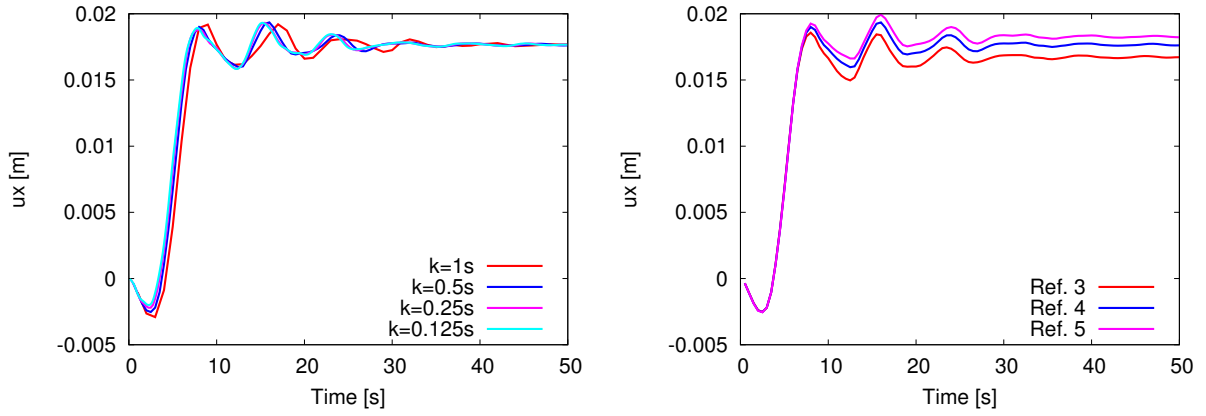


Figure 5: Example 1: Convergence tests in time (left) and space (right) for the point value $\hat{u}_x(1, 0.75)$.

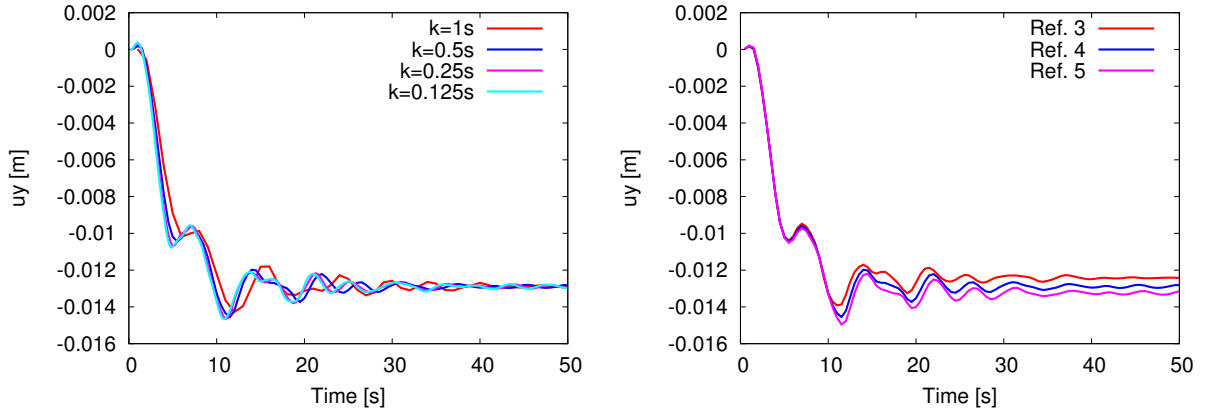


Figure 6: Example 1: Convergence tests in time (left) and space (right) for the point value $\hat{u}_y(1, 0.75)$.

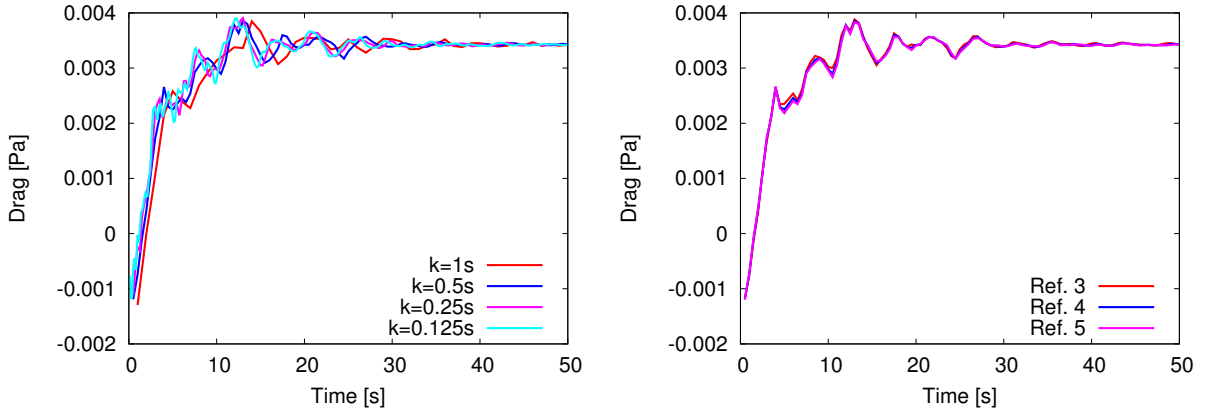


Figure 7: Example 1: Convergence tests in time (left) and space (right) for the drag.

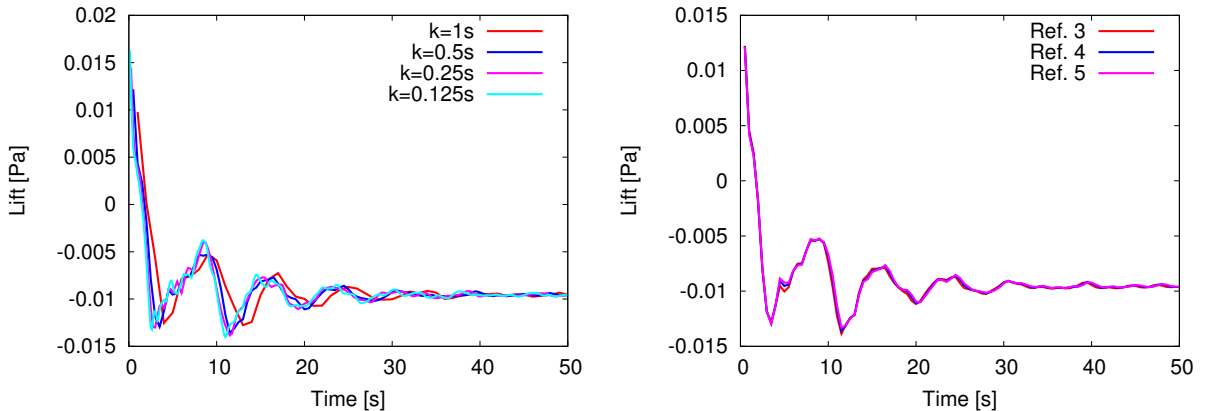


Figure 8: Example 1: Convergence tests in time (left) and space (right) for the lift.

5.2. Example 2: A fixed fracture, higher flow, large solid deformation

In this second test, the inflow is increased resulting in a large deformation of the elastic obstacle. The main goal are sensitivity studies using different μ_v in order to analyze the influence of solid damping on quantities of interest and the Newton performance; we remind Remark 3.4 in which our purpose to use solid damping has been explained. Since damping effects can also be achieved by working with a corresponding time-stepping scheme, namely the strongly A-stable backward Euler scheme, comparisons with shifted Crank-Nicolson and backward Euler are carried out.

Configuration. The geometry and notation are provided in Figure 9. The number of mesh cells and degrees of freedom are the same as in the first example.

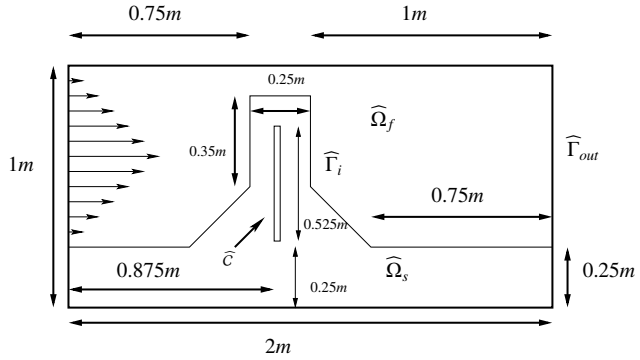


Figure 9: Example 2: Notation of domains and boundaries.

Boundary and initial conditions. The boundary conditions are the same as in the first example.

A parabolic inflow velocity profile is given on $\hat{\Gamma}_{in}$ by

$$v_f(0, y) = \bar{U}(y - 1)(y - 0.25), \quad \bar{U} = 2ms^{-1}.$$

For $t < 2.0s$, $v_f(0, y)$ is scaled with $\frac{1-\cos(\frac{\pi}{2}t)}{2}$ in order to have a smooth inflow profile.

Parameters. For the fluid we use $\varrho_f = 1kgm^{-3}$, $\nu_f = 10^{-2}m^2s^{-1}$. The elastic solid is characterized by $\varrho_s = 1kgm^{-3}$, $\nu_s = 0.2$, and $\mu_s = 10^3kgm^{-1}s^{-2}$. In fact the solid density is now the same as for the fluid and thus one can expect that the added-mass effect [19] is present and hence monolithic FSI-solvers are preferable. The fracture pressure is $\hat{p}_F = 10Pa$ (for the choice of this value, we refer to the discussion below). The model parameter $\varepsilon = 0.044 = h_{coarse}$ is fixed in all computations as well as $\kappa = 10^{-10}$. Furthermore, $\gamma = 10^2$ and $G_c = 1N/m$. The (absolute) Newton tolerance is chosen as 10^{-10} . Two time step sizes $k = 1s$ and $k = 0.125s$ are chosen and the total time is $T = 20s$. The solid damping parameters are chosen as $\mu_v = 0, 1, 10, 10^2, 10^3$. The maximal velocity is $v_{max} = 1.38m/s$. The lowest channel width is $D = 0.15m$. Thus, the Reynolds number is $Re = \frac{v_{max}D}{\nu_f} = 20.7$.

Quantities of interest. As goal functionals we observe

- the point displacement $\hat{u}_x(1, 0.85)$;
- $\min(\hat{J})$, measuring the quality of the ALE mapping;
- the number of Newton iterations w.r.t. to solid damping and w.r.t. to time-stepping.

Discussion of our findings. The numerical solution is visualized in Figure 10. We also see that the fracture is squeezed (see Figure 11) and thus the pressure \hat{p}_F in the fracture must be high enough such that a collapse is avoided. This is evident from a physical point of view. On the other hand, \hat{p}_F must not be too high since the fracture would burst otherwise. The correct pressure \hat{p}_F is heuristically obtained.

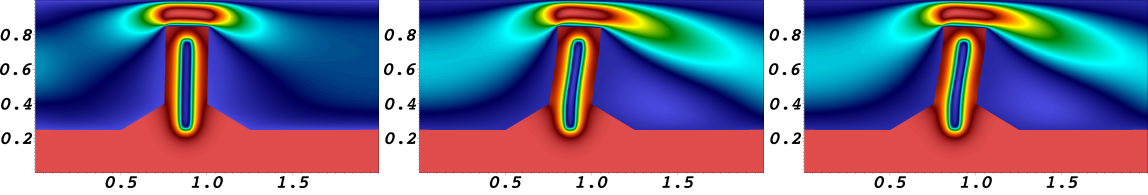


Figure 10: Example 2: Sequence of snapshots at times $T = 1, 10, 20$ s of the magnitude of the flow field (with a maximum of 1.38m/s flow velocity) and the fracture path. The latter one is represented by the phase-field variable $\hat{\varphi}$. The fracture is characterized by $\hat{\varphi} = 0$ (blue region in the brown solid part).

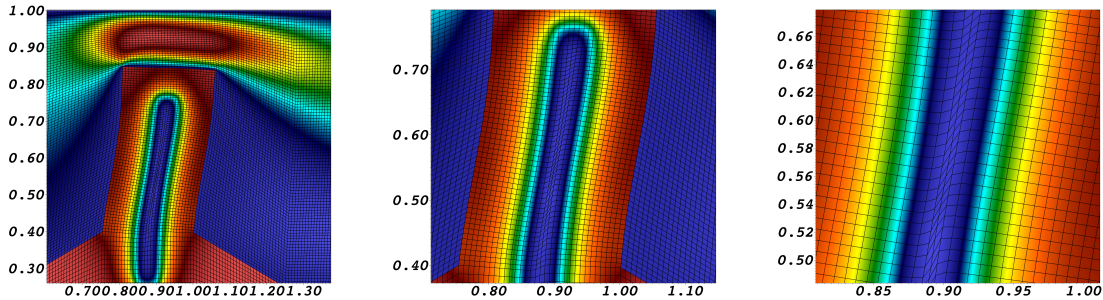


Figure 11: Example 2: Sequence of zoom-ins at $T = 20$ s with a focus on the damaged obstacle. In the right plot, we observe that the fracture is squeezed in the middle, which can be seen from the distorting mesh cells in the very middle of the (blue-colored) fracture. This is a critical aspect since the pressure \hat{p}_F must be sufficiently high in order to avoid a collapse (too much compression) of the fracture, but also \hat{p}_F should not be too high in order to avoid bursting of the obstacle.

The main aim in the following investigation is to better understand solid damping. In Figure 12 we compare the shifted Crank-Nicolson scheme with backward Euler time-stepping using a large time step size $k = 1\text{s}$ and $\mu_v = 10^3$. Both lead to the same curves for the u_x displacements of the obstacle tip. Using a smaller time step size $k = 0.125\text{s}$ yields very similar findings that are not shown here. Next we use smaller damping $\mu_v = 10^2, 10^1, 10^0, 0$. First we notice that neither backward Euler nor the shifted Crank-Nicolson scheme work on finer meshes, but only on Ref. 3. The Newton performance for Ref. 3 is shown in Table 1. Since also backward Euler (which is generally robust and has a strong damping influence itself) does not work on finer meshes, we test a procedure that is motivated by [54, 64] in which the Crank-Nicolson scheme is ‘started’ with backward Euler steps in the case of rough initial data. Here, we adapt this idea and ‘start’ the computation (not by combining two time-stepping schemes but) by using high solid damping $\mu_v = 10^3$ in the initial step and setting μ_v to a smaller value at all further times. This approach now allows to work on finer meshes. These findings are summarized in Figure 13 in which for the shifted Crank-Nicolson scheme a sequence of different μ_v are adopted. A comparison between backward Euler and shifted Crank-Nicolson for $\mu_v = 10^3$ at the beginning and then setting $\mu_v = 0$ is shown in the right plot of Figure 13. In particular, we observe that already one order of magnitude less, namely $\mu_v = 10^2$, leads to a deflection of the obstacle that is close to the undamped ($\mu_v = 0$) setting. Studies of the ALE-mesh regularity can be observed in Figure 14. Finally, the number of Newton iterations at certain time instances for both time-stepping schemes are listed in Table 2. Here, the shifted Crank-Nicolson scheme shows not only a better performance (somewhat unexpected) but moreover backward Euler requires to work with a modified Newton solver that allows for a temporary increase of the residual. These findings are shown in Figure 15. Therein, we also see (as expected) that Newton convergence is achieved faster when employing smaller time step sizes. Drawing a conclusion of this example, we observe that solid damping has clearly an influence on the numerical findings but is also indispensable for the nonlinear solver in order to converge. However, damping for a fixed fracture is much less important than for a propagating fracture as investigated in the Examples 3-5. It thus remains an open question whether solid damping in the presence of pressurized dynamic fractures can be completely removed for FSI-PFF problems.

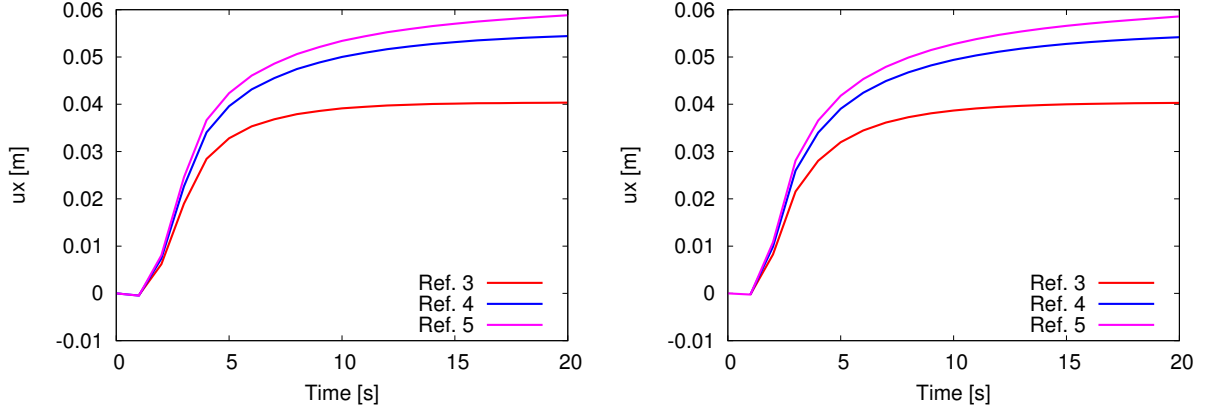


Figure 12: Example 2: Display of $\hat{u}_x(1, 0.85)$. CNs (left) and BE (right) time-stepping each with $k = 1\text{s}$ and $\mu_v = 10^3$. Using a smaller time step size $k = 0.125\text{s}$ yields very similar findings that are not shown here.

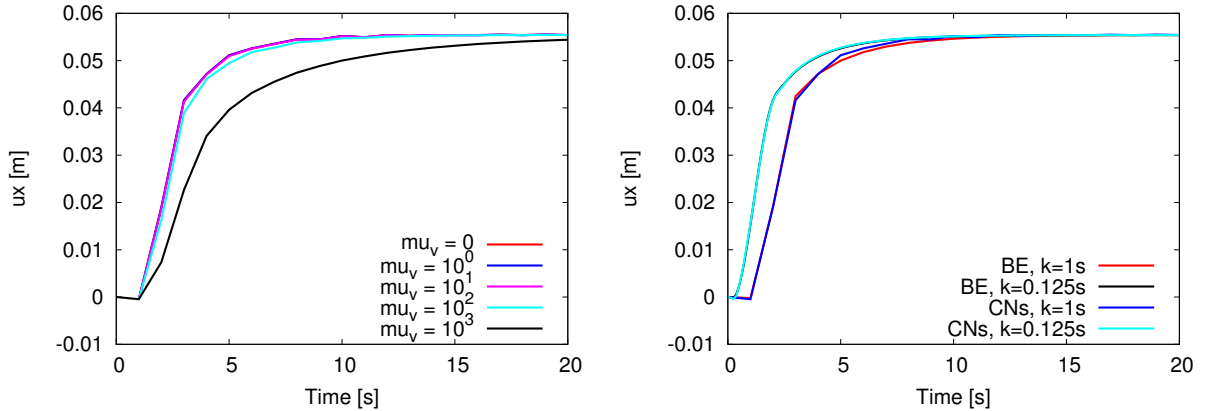


Figure 13: Example 2: Display of $\hat{u}_x(1, 0.85)$. CNs with $k = 1\text{s}$ and different damping parameters μ_v (left). At right, the refinement level is 4 and $\mu_v = 0$ (initialized in the first time step with $\mu_v = 10^3$).

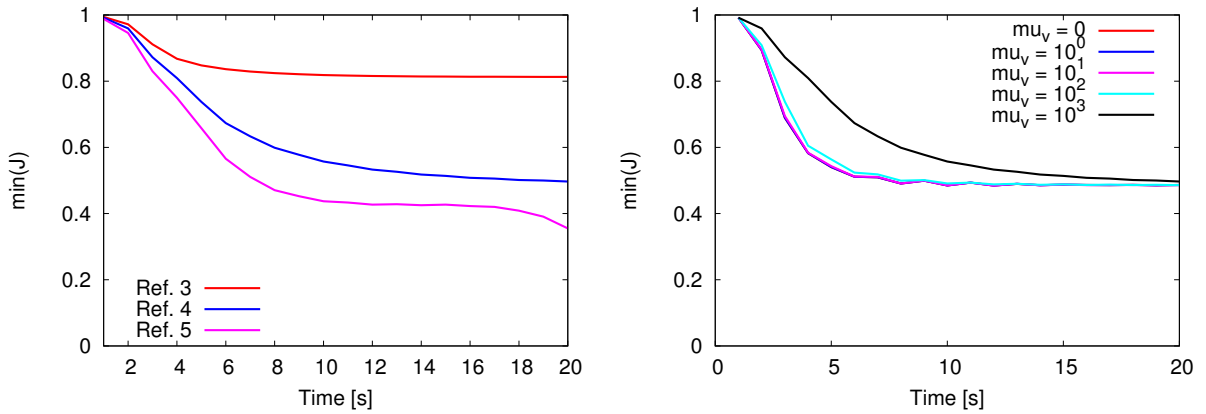


Figure 14: Example 2: Display of $\min(\hat{J})$. At left spatial convergence is shown using the shifted Crank-Nicolson scheme, $k = 1\text{s}$ and $\mu_v = 10^3$ and on the right sensitivity (on refinement level 4) with respect to the damping parameter μ_v .

Table 1: Example 2: Number of Newton iterations with respect to μ_v on Ref. 3 and using the shifted Crank-Nicolson scheme with $k = 1s$. For $\mu_v < 10^3$ this respective μ_v is used from the very beginning of the computation. On finer meshes, Newton's method will not converge for this example; results are obtained when $\mu_v = 10^3$ is used in time step 0 and afterwards μ_v is set to a respective smaller value as shown in Table 2.

μ_v	$T = 4s$	$T = 10s$	$T = 20s$
1	10	23	29
10	10	14	14
100	9	9	9
1000	8	7	8

Table 2: Example 2: Number of Newton iterations (stopping at a tolerance of $TOL < 10^{-10}$) on Ref. 4 for backward Euler and shifted Crank-Nicolson time-stepping, two different time step sizes, $\mu_v = 10^3$ in time step 0 and $\mu_v = 0$ for all further times.

TS	$k[s]$	$T = 4s$	$T = 10s$	$T = 20s$
BE	1	18	18	16
CNs	1	11	13	12
BE	0.125	15	14	12
CNs	0.125	8	7	5

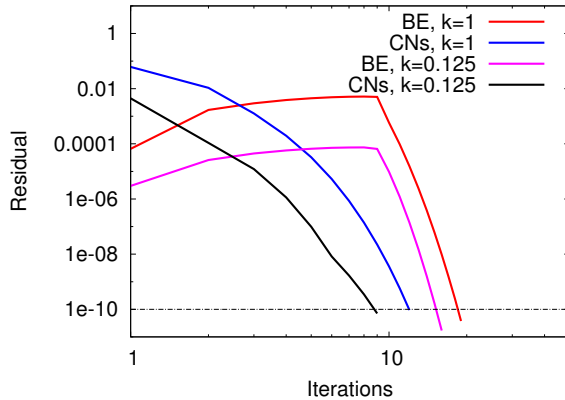


Figure 15: Example 2: Newton convergence at $T = 4s$ for backward Euler and shifted Crank-Nicolson time-stepping, two different time step sizes, $\mu_v = 10^3$ in time step 0 and μ_v for all further times. Using the backward Euler scheme, we detect first a (temporary) increase of the residual norm after which convergence follows. This shows the necessity to work with a modified Newton solver.

5.3. Example 3: A propagating fracture, high flow, and moderate solid deformation

In this third test we consider a propagating fracture in the solid part, which is achieved by increasing the pressure inside the fracture. The geometric configuration is the same as in Section 5.1. The inflow is increased to $\bar{U} = 10ms^{-1}$. However, we notice that the material parameters are also increased in their values. Consequently, the solid is now very stiff and less deformed than in the first two examples.

Parameters. For the fluid we use $\varrho_f = 1kgm^{-3}$, $v_f = 10^{-2}m^2s^{-1}$. The elastic solid is characterized by $\varrho_s = 10kgm^{-3}$, $v_s = 0.2$, $\mu_s = 10^6kgm^{-1}s^{-2}$. The fracture pressure does now linearly increase with time:

$$\hat{p}_F(t) = 5.0 \times 10^2 + t * 5.0 \times 10^2,$$

where $0 \leq t \leq T$ denotes the current time. The end time value T is not specified and the computation is terminated when the fracture reaches the bottom boundary. This event takes place around $T \approx 8s$. The time step size is chosen as $k = 0.25s$ for most comparisons. But we also perform time convergence studies for $k = 0.5s, 0.25s, 0.125s$. This time,

we use the backward Euler time stepping scheme ($\theta = 1$) providing better numerical stability. The investigation of accuracy and performance of other time-stepping schemes for our setting with propagating fractures is left for future research.

The model parameter $\varepsilon = 0.044 = h_{coarse}$ is again fixed in all computations as well as $\kappa = 10^{-10}$. Furthermore, $\gamma = 100$ and as before $G_c = 1N/m$. For propagating fractures, solid damping is even more important than for the fixed fracture in Example 2. Here, they are chosen as $\mu_v = 10^5$ and $\lambda_v = \frac{2}{3}\mu_v$. For a brief inspection of Newton's performance we also choose $\mu_v = 10^4$ in Table 3. As discussed in Example 2, a lower value does less suppress solid waves, but also downgrades the Newton performance yielding more iterations per augmented Lagrangian step. The maximal velocity is $v_{max} = 1.25m/s$. The lowest channel width is $D = 0.25m$. Thus, the Reynolds number is $Re = 31.25$.

Quantities of interest. We observe:

- the displacement $\hat{u}_x(1, 0.75)$;
- the stress in x -direction (drag) on $\widehat{\Gamma}_i$;
- evaluation of COD = $\int_{\{0 \leq x \leq 2; y=0.4375\}} \hat{u}_s \widehat{\nabla} \hat{\varphi} d\hat{s}$, which is related to phase-field fracture modeling;
- the fracture length;
- number of average Newton iterations (Aver. Iter.) in two time slots in order to study the robustness of the nonlinear solver with respect to solid damping.

Except for the last task, all quantities of interest are investigated for $\mu_v = 10^5$.

Discussion of our findings. We note that solid damping is indispensable to achieve convergence of the nonlinear solver. The results of Newton iterations are shown in Table 3. Indeed, $\mu_v = 10^4$ yields a bad performance and fails on the finest mesh level. As visualized in Figure 16, the fracture grows perpendicular to the FSI interface and towards the bottom of the configuration. That the fracture does not grow further inside the obstacle towards the FSI interface is due to the fact that $\hat{\varphi} = 1$ is chosen on $\widehat{\Gamma}_i$. Later, in Section 5.5, we weaken this condition and will find that the fracture can indeed interact with the FSI-interface. As in the other tests, the emphasize in this study is on numerical stability for this specific model choice with a propagating fracture and hence on stable results for different time step sizes k and h . Quantitative results of the spatial convergence of the stresses along the FSI-interface are shown in Table 4. Here, we observe convergence; however the variations are quite small since the solid is very stiff.

A visualization of the crack opening displacement COD and corresponding convergence tests are found in Figure 17 and 19. Our analysis is finished by convergence tests of $\hat{u}_x(1, 0.75)$ and the drag and fracture length (see Figures 18 and 20).

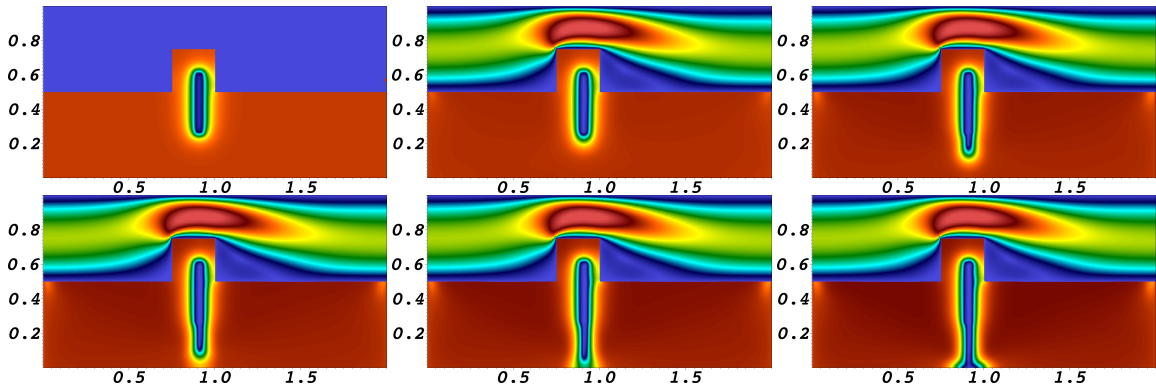


Figure 16: Example 3: Sequence of snapshots at times $T = 0, 5, 6.5, 7, 7.5, 8s$ of the magnitude of the flow field (with a maximum of $1.25m/s$ flow velocity) and the fracture path. The latter one is represented by the phase-field variable $\hat{\varphi}$. The fracture is characterized by $\hat{\varphi} = 0$ (blue).

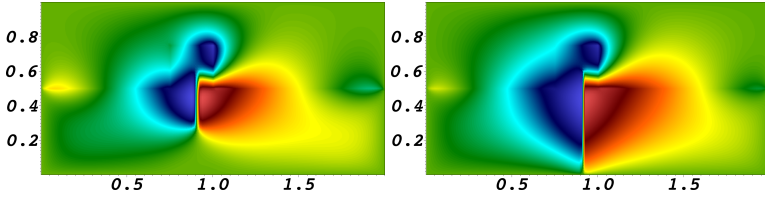


Figure 17: Example 3: Display of the x -displacements (also known as the so-called crack opening displacement (COD); perpendicular to the fracture orientation). At $T = 0$ the COD varies between -0.1mm and 0.1mm . At the final time $T = 8\text{s}$, the COD varies between -0.8mm and 0.9mm .

Table 3: Number of Newton iterations using $k = 0.25\text{s}$ for $\mu_v = 10^5$ and $\mu_v = 10^4$. In the first time slot $0 \leq t \leq 5\text{s}$ the fracture does not yet increase in its length. In the second time slot, the fracture propagates until the bottom boundary is reached at $T = 8\text{s}$.

Cells	DoFs	Aver. Iter $0 \leq t \leq 5\text{s}$	Aver. Iter $5 \leq t \leq 8\text{s}$	Aver. Iter $0 \leq t \leq 5\text{s}$	Aver. Iter $5 \leq t \leq 8\text{s}$
2048	41829	5	8	5	13
8192	165573	5	10	6	17
32768	658821	6	12	7	--

Table 4: Drag and lift evaluation at two time instances $T = 2\text{s}$ and $T = 8\text{s}$ for all three mesh refinement levels.

Cells	DoFs	Drag at 2s	Drag at 8s	Lift at 2s	Lift at 8s
2048	41829	0.4725	0.4080	-1.4385	-0.9069
8192	165573	0.4722	0.4076	-1.4332	-0.9037
32768	658821	0.4722	0.4079	-1.4332	-0.9032

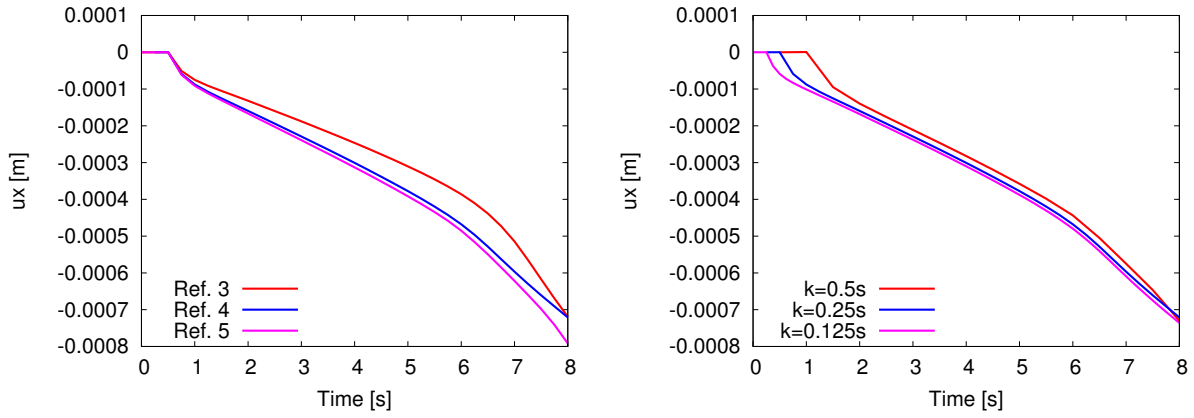


Figure 18: Example 3: Comparison of $u_x(1, 0.75)$ in space and time.

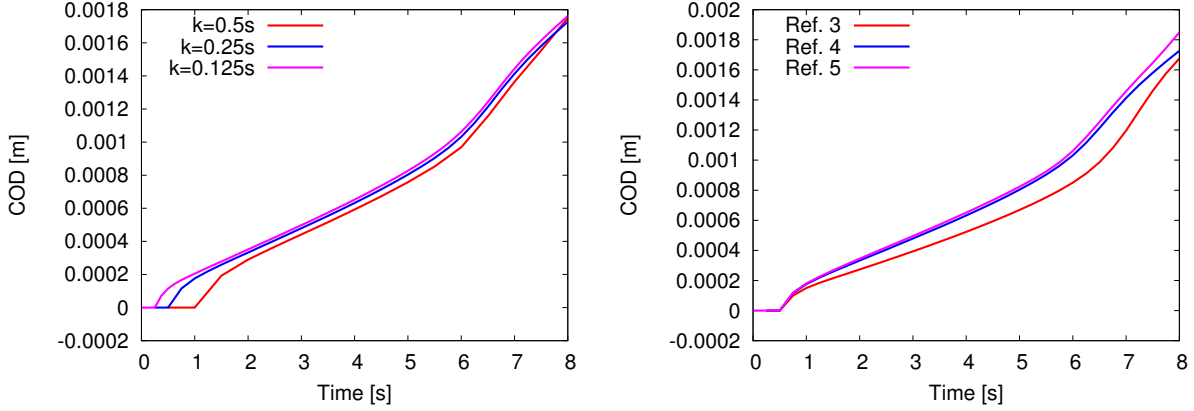


Figure 19: Example 3: Convergence in time and space of the crack opening displacement COD.

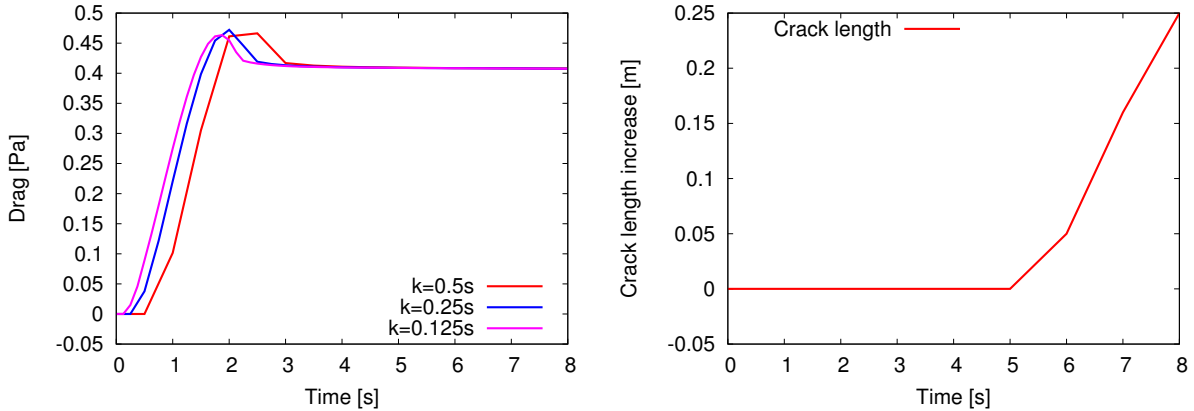


Figure 20: Example 3: Convergence in time for the drag on the mesh level Ref. 4 (left) and increase in fracture length measured on refinement level 5 for $k = 0.25\text{s}$. Convergence studies for the fracture length are provided in Section 5.4.

5.4. Example 4: Multiple fractures, high flow, and moderate solid deformation

In this example, we consider three, non-aligned, fractures \widehat{C}_1 , \widehat{C}_2 and \widehat{C}_3 in the initial configuration. These fractures are again pressurized. The aim is again to observe propagating fractures and whether all three fracture will increase their length. This study is again carried out for different spatial mesh levels and different time step sizes.

Configuration. The configuration is displayed in Figure 21 and the boundary and initial conditions are the same as in Section 5.3. Moreover, the geometric data for \widehat{C}_1 , \widehat{C}_2 and \widehat{C}_3 are provided in this figure.

Parameters. The driving pressure force and all remaining choices of parameters, spatial and temporal discretization are kept as in Section 5.3.

Quantities of interest. We measure:

- the fracture length (of the vertical fracture);
- the line integral on $\int_{[0 \leq x \leq 2; y=0.4375]} \hat{u} \nabla \hat{\varphi} d\hat{s}$.

We notice that the line integral is the same as in Section 5.3 but cannot be interpreted any more as the crack opening displacement since we also cut the other two fractures in non-perpendicular direction.

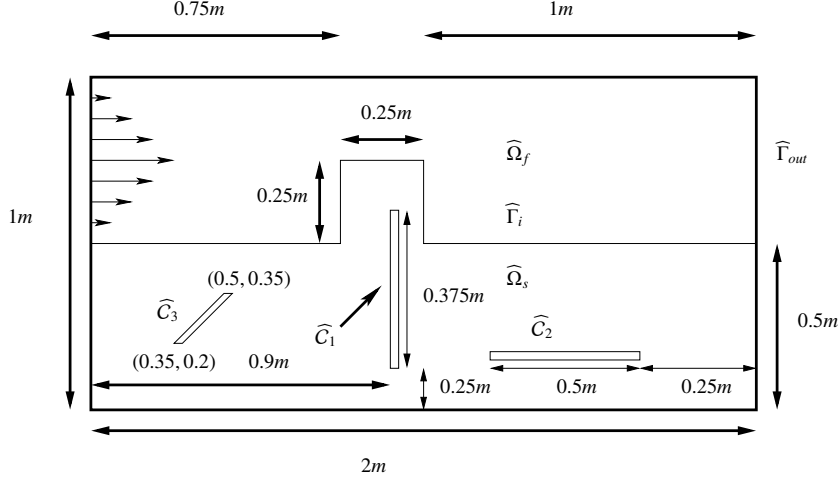


Figure 21: Configuration of Section 5.4 with the prescription of three initial fractures \widehat{C}_1 , \widehat{C}_2 and \widehat{C}_3 .

Discussion of our findings. It is striking that only the fracture vertical to the FSI interface grows as visualized in Figure 22. Our explanation is as follows: it is well known that pressurized fractures are tensile fractures and propagate perpendicular to the least principle stress, e.g., [4]. According to these results, the least stresses are found at the right and left boundaries whereas high stresses take place at the FSI interface. The displacement fields are illustrated in Figure 23. This section is concluded by convergence tests in time and space for the line integral $\int_{[0 \leq x \leq 2; y=0.4375]} \hat{u} \nabla \hat{\varphi} d\hat{s}$ (shown in Figure 24) and the fracture length as plotted in Figure 25.

Remark 5.1. Despite the fact that the fractures do not join in this example, we emphasize that phase-field in general does allow this feature. We exemplarily refer to multiphysics fractures in subsurface modeling; namely fluid-filled fractures in poroelasticity [60, 61] (2D) or [53, 57] for 3D configurations.

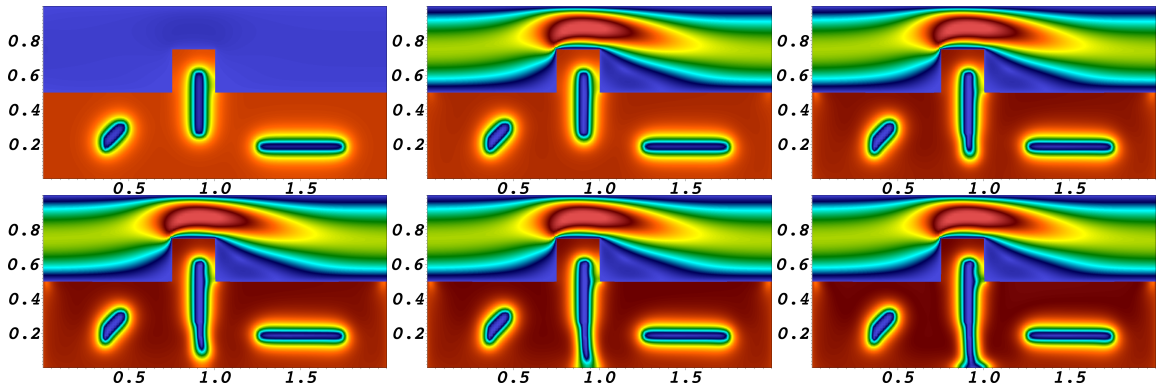


Figure 22: Example 4: Sequence of snapshots at times $T = 0, 7.5, 8.0, 8.5, 9.0$ of the magnitude of the flow field and the fracture path. The latter one is represented by the phase-field variable $\hat{\varphi}$. The fracture is characterized by $\hat{\varphi} = 0$ (blue).

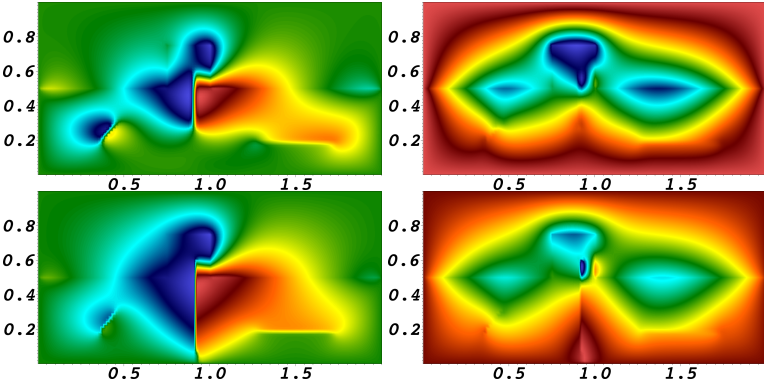


Figure 23: Example 4: Display of the x and y displacements at the initial time $T = 0\text{s}$ and $T = 9\text{s}$ where the fracture reaches the lower boundary. The x -displacements vary in a range of -0.9mm (blue) to 1.1mm (dark red). The y -displacements vary in a range of -1.3mm (blue) to 0.3mm (red).

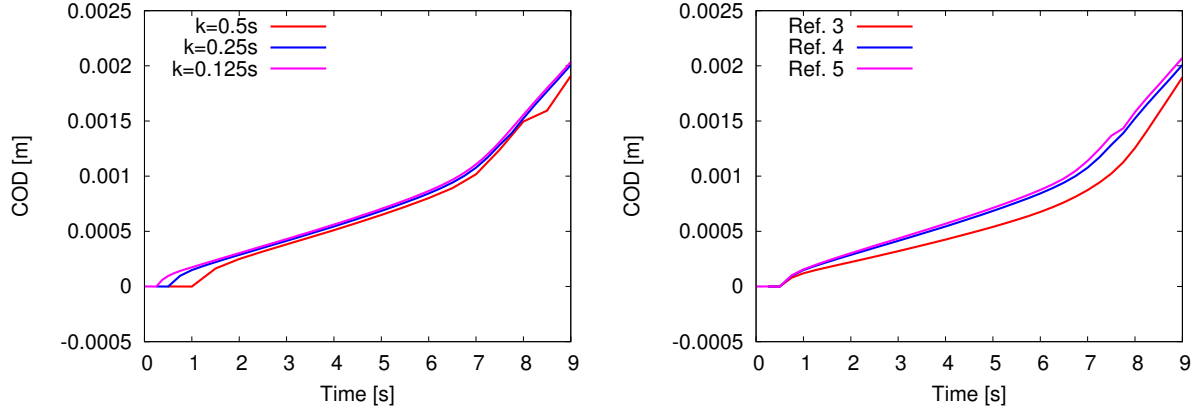


Figure 24: Example 4: Convergence studies in time and space of the line integral. Convergence in time is measured on the middle mesh level Ref. 4 and convergence in space is performed with the time step size $k = 0.25\text{s}$.

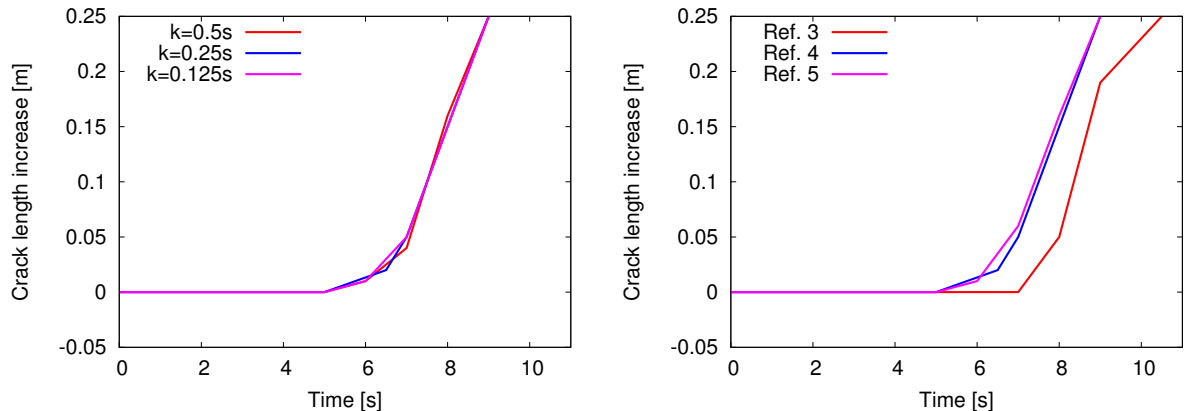


Figure 25: Example 4: Convergence studies in time and space of the increase in fracture length. Convergence in time is measured on the middle mesh level Ref. 4 and convergence in space is performed with the time step size $k = 0.25\text{s}$. We emphasize that the final length increase of 0.25m means that the fracture reaches the bottom boundary.

5.5. Example 5: High flow, large solid deformation, and evolving fracture(s)

In this final example, we consider two settings based on the configuration of Example 2. In contrast to the Examples 3 and 4, the solid is now smoother resulting in a higher deformation of the obstacle. Here, we do not impose $\hat{\varphi} = 1$ on $\widehat{\Gamma}_i$, which allows the fracture to interact with this boundary. The inflow is $\bar{U} = 2\text{m/s}$ (Example 5a) and $\bar{U} = 1\text{m/s}$ (Example 5b). Moreover, the fracture will evolve and interact with the FSI interface. Since the flow is sufficiently high in order to have a significant solid deformation, both effects, interaction of fluid and solid and fracture propagation, take place.

Configuration. The geometry and notation are provided in Figure 26. In Example 5a, one fracture (left subfigure in Fig. 26) is initially prescribed and in Example 5b, two initial fractures (right subfigure in Fig. 26) are given.

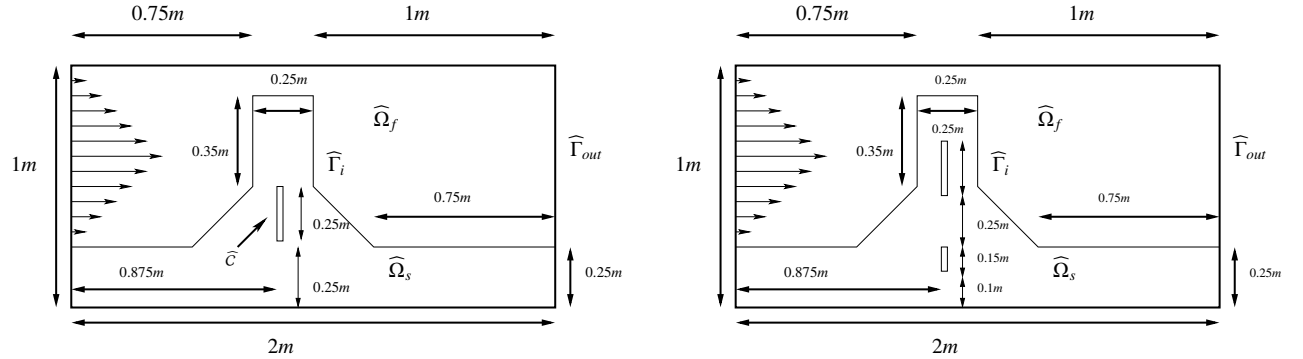


Figure 26: Examples 5a/b: Configurations and initial fractures.

Parameters. For the fluid we use $\varrho_f = 1\text{kgm}^{-3}$, $v_f = 10^{-2}\text{m}^2\text{s}^{-1}$. The elastic solid is characterized by $\varrho_s = 1\text{kgm}^{-3}$, $\nu_s = 0.2$, $\mu_s = 10^3\text{kgm}^{-1}\text{s}^{-2}$. The model parameter $\varepsilon = 0.044 = h_{coarse}$ is fixed in all computations as well as $\kappa = 10^{-10}$. Furthermore, $\gamma = 10^2$ and $G_c = 1\text{N/m}$. The time step size is $k = 1\text{s}$. As time stepping scheme, we use the implicit Euler scheme. The solid damping parameter is $\mu_v = 10^3$. The fracture pressure linearly increases with time:

$$\hat{p}_F(t) = 10^2 + t * 1.0 \times 10^2,$$

where $0 \leq t \leq T$ denotes the current time. In Example 5a, we have $v_{max} = 1.36\text{m/s}$, thus $Re = 20.4$. The maximal velocity in Example 5b is $v_{max} = 0.55\text{m/s}$. Thus, the Reynolds number is $Re = \frac{v_{max}D}{v_f} = 8.25$. The lower inflow in Example 5b is necessary since the fracture is located in the top of the obstacle, which is therefore much more sensitive to the flow.

Quantities of interest. The goal functionals are:

- the crack pattern;
- u_x and u_y displacements in $(1.0, 0.85)$;
- drag/lift acting on the FSI-interface;
- $\min J(u)$.

Discussion of our findings (Example 5a). In this example, we observe that the increasing fracture pressure causes a damaged zone left from the initial fracture; see Figure 27 and 28. Specifically, a new damaged zone at the FSI-interface develops and then propagates. This causes a significant deformation of the obstacle. Secondly, this example shows that fractures can interact with the FSI-interface. But as already discussed, in this paper we do not address modeling how the Navier-Stokes pressure might be linked to the fracture pressure; see Remark 3.3. Finally, the behavior of the displacements and the normal stresses are depicted in Figure 29.

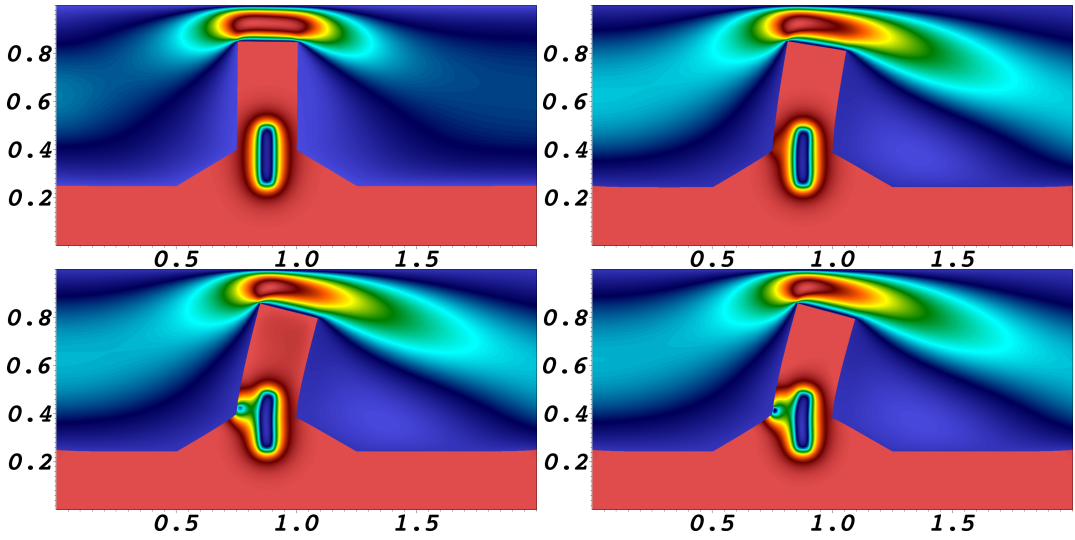


Figure 27: Example 5a: Sequence of snapshots at times $T = 1, 7, 9, 10$ s of the magnitude of the flow field and the fracture path. The latter one is represented by the phase-field variable $\hat{\varphi}$. The fracture is characterized by $\hat{\varphi} = 0$ (blue part in the brown zone).

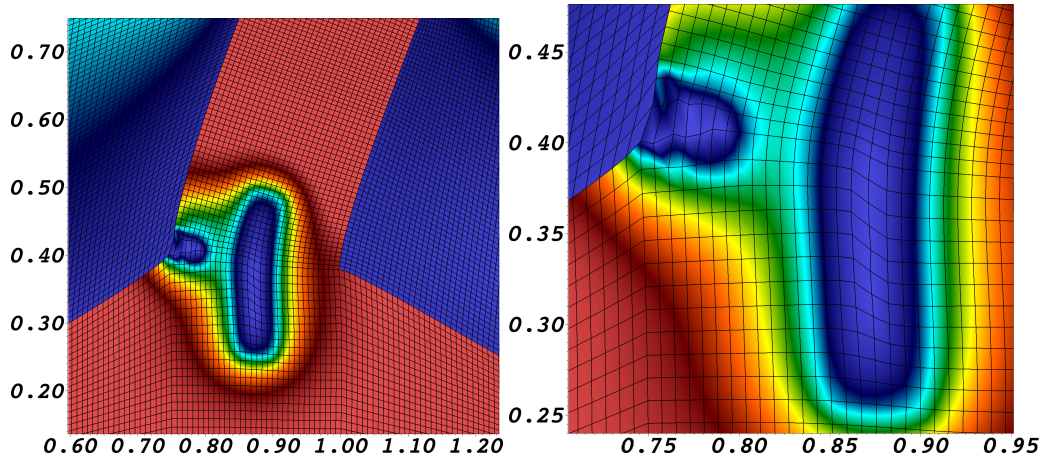


Figure 28: Example 5a: Zoom-in at $T = 10$ s to the obstacle with the fracture and the new damage at the FSI-interface.

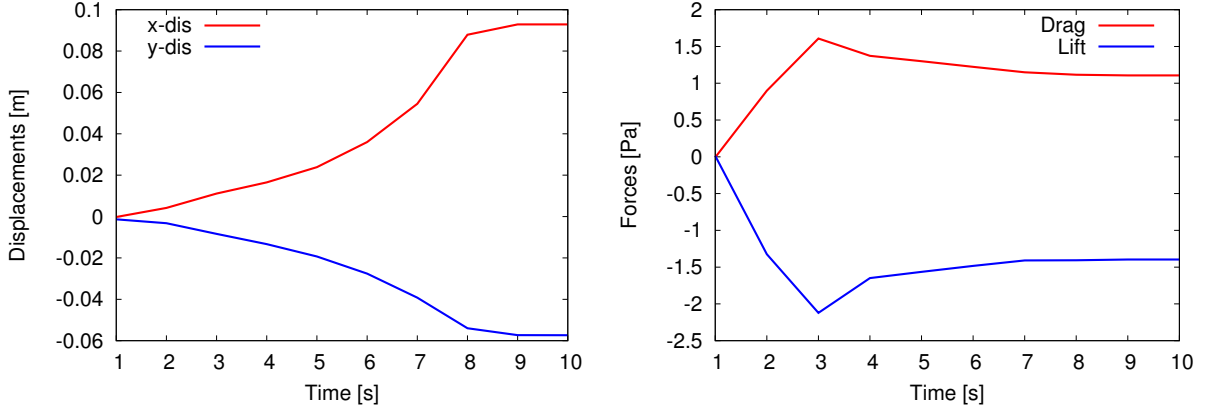


Figure 29: Example 5a: Evolution of the displacements (at left) and the surface forces, drag and lift (at right).

Discussion of our findings (Example 5b). In this example, we finally observe a fracture that penetrates at $T = 12\text{s}$ the entire obstacle as pictured in Figure 30. In the next time step $T = 13\text{s}$ - not shown though - the obstacle will be completely cracked. However, this solution is non-physical since $\min J(u) < 0$ and Newton's method did not converge anymore to the tolerance. Such a sudden cracking might be due to the brittle fracture model and can be therefore expected. Up to the total damage $T < 13\text{s}$, we observe again spatial convergence for different goal functionals as depicted in the Figures 31, 32 and Table 5. In conclusion, these two final Examples 5a and 5b show that the proposed method and numerical solution can be indeed adopted for large solid deformations and evolving fractures.

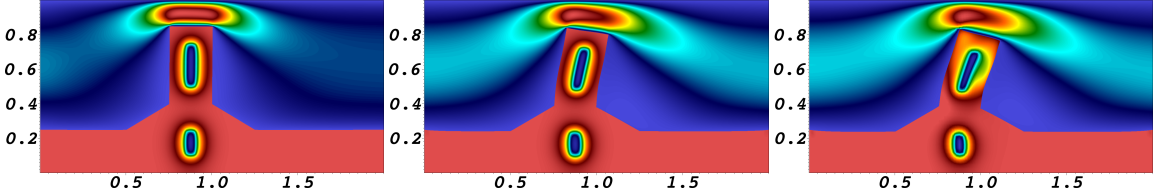


Figure 30: Example 5b: Sequence of snapshots at times $T = 1, 10, 12\text{s}$ of the magnitude of the flow field and the fracture path. The latter one is represented by the phase-field variable $\hat{\varphi}$. The fracture is characterized by $\hat{\varphi} = 0$ (blue region in the brown solid). Moreover, the fracture penetrates at $T = 12\text{s}$ the entire obstacle (green/yellow region).

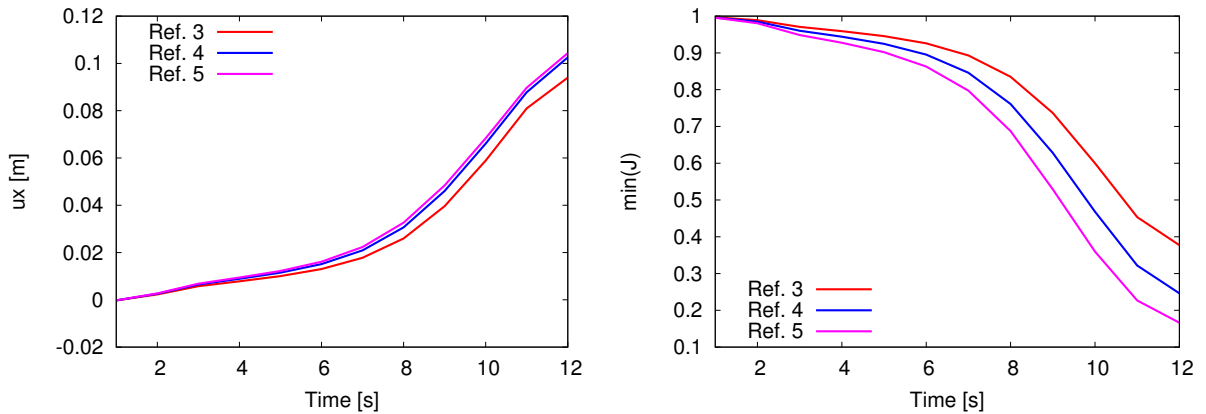


Figure 31: Example 5b: Evolution of the \hat{u}_x displacements (at left) and the minimal $J(\hat{u})$ (at right).

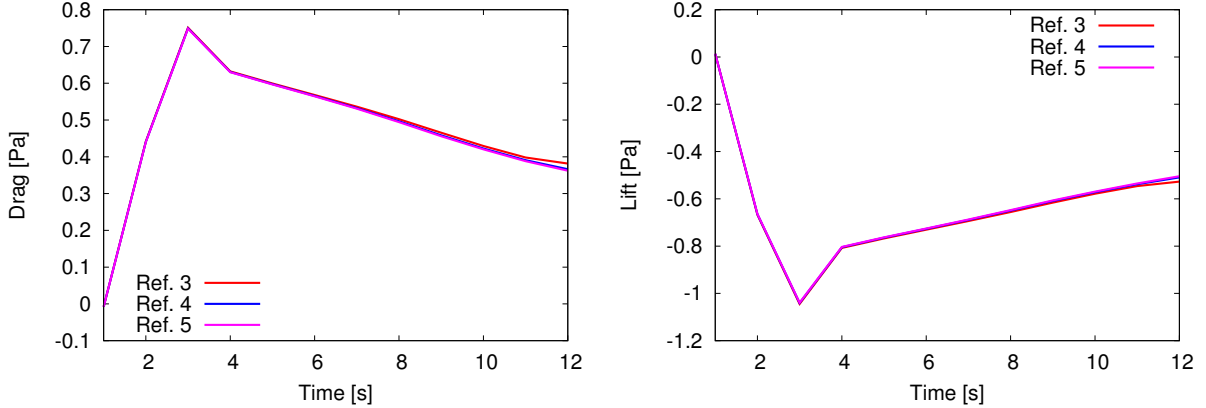


Figure 32: Example 5b: Evolution and convergence studies of drag and lift.

Table 5: Example 5b: Drag and lift evaluation at two time instances $T = 3\text{s}$ and $T = 12\text{s}$ for Ref. 3-5.

Cells	DoFs	Drag at 3s	Drag at 12s	Lift at 3s	Lift at 12s
2048	41829	0.7511	0.3816	-1.0446	-0.5272
8192	165573	0.7492	0.3662	-1.0408	-0.5096
32768	658821	0.7484	0.3617	-1.0390	-0.5045

6. Conclusions

In this work, fluid-structure interaction (FSI) has been coupled with a phase-field fracture (PFF) approach and a model for pressurized-fractures in elastodynamics. To the best of our knowledge, this paper constitutes the first attempt to couple fluid-structure interaction with phase-field fracture.

The proposed framework is formulated in a variational-monolithic ALE-setting that ensures high accuracy of the coupling conditions. Details on mathematical modeling, derivation of interface conditions, enforcement of the inequality constraint, and on temporal and spatial discretization are provided. The resulting nonlinear problem requires a crucial modification of the nonlinear solver, here Newton's method, which allows for a temporary increase (in the first Newton steps) of the residual. As already outlined in [52, 51] the dynamic fracture model needs to be supplemented with a dissipation term. In Example 2, a technique is proposed in which solid damping is applied only in the initial time step, helping to initialize a smooth solution that allows to reduce damping afterwards. In the Examples 3-5, it turns out that indeed this term is crucial for propagating fractures and as such remains an open question whether solid damping can be removed.

Summarizing the theoretical and algorithmic parts, this paper contains several novelties that have not been addressed in existing literature such as a phase-field model for dynamic pressurized fracture as part of the solid system, formulating phase-field fracture in terms of ALE coordinates, and interface conditions for coupling the fractured solid to the incompressible Navier-Stokes equations. With regard to the numerical discretization, A-stable, but less dissipative time-stepping for energy conservation of the hyperbolic solid equation, and higher order spatial discretization for the Navier-Stokes equations must be considered, as well as state-of-the-art methods for phase-field fracture modeling. Having both frameworks available is non-trivial and therefore the biggest endeavor in this work.

In the numerical examples it has been shown that the model is computationally stable while observing convergence of various goal functionals. These goal functionals are typical quantities of interest such as displacements of the obstacle, normal stresses, the minimal determinant of the deformation gradient, the crack opening displacement and the fracture length. Another difficulty that we faced was that the fracture (Example 2) tends to collapse (i.e., compressed) when the exerted force of the fluid on the obstacle is too high in comparison to the pressure inside the fracture. This is clear from a physical point of view but is a delicate issue in numerical simulations. Therefore, we

choose heuristically a fracture pressure that fulfills both requirements: preventing too much compression by choosing the fracture pressure sufficiently high, but also preventing the fractured solid obstacle to burst by choosing the fracture pressure not too high though.

Having established computational stability of this basic model is very important for further numerical developments such as other coupling schemes and iterative linear solvers. Other future directions are concerned with modeling and applications: adding the solid acceleration term to the phase-field fracture model is of current interest in other fields, e.g., in geophysical applications. The (probably) most appealing topic is the phase transition on the FSI-interface when the fracture reaches this region (see Example 5a) and its subsequent coupling to the fracture pressure. The next further extension would be to describe Stokes or Navier-Stokes flow in the fracture and its coupling to the channel flow equation. Here phase-field can serve as an indicator function which determines the fracture location in which the fracture-Navier-Stokes equation should be described. A similar idea for coupling Darcy flow in the fracture and the surrounding medium has been proposed in [60].

Acknowledgments

I wish to thank Dr. Huidong Yang (RICAM Linz; now in Graz) for discussions in the middle of the preparation of the first version of this paper, which helped to identify an important error in the programming code. And I want to thank him a second time for a discussion on the ALE crack irreversibility condition in the first revised version of the paper. Moreover, I wish to thank the anonymous reviewers for their careful reading and useful suggestions in a couple of review rounds.

References

References

- [1] G. Allaire, F. Jouve, and N. V. Goethem. Damage and fracture evolution in brittle materials by shape optimization methods. *Journal of Computational Physics*, 230(12):5010 – 5044, 2011.
- [2] L. Ambrosio and V. Tortorelli. Approximation of functionals depending on jumps by elliptic functionals via γ -convergence. *Comm. Pure Appl. Math.*, 43:999–1036, 1990.
- [3] L. Ambrosio and V. Tortorelli. On the approximation of free discontinuity problems. *Boll. Un. Mat. Ital. B*, 6:105–123, 1992.
- [4] T. Anderson. *Fracture mechanics: Fundamental and Applications, 3rd edition*. CRC Press, Boca Raton, London, New York, Singapore, 2005.
- [5] M. Artina, M. Fornasier, S. Micheletti, and S. Perotto. Anisotropic mesh adaptation for crack detection in brittle materials. *SIAM J. Sci. Comput.*, 37(4):B633–B659, 2015.
- [6] W. Bangerth, R. Hartmann, and G. Kanschat. deal.II – a general purpose object oriented finite element library. *ACM Trans. Math. Softw.*, 33(4):24/1–24/27, 2007.
- [7] W. Bangerth, T. Heister, G. Kanschat, and M. Maier. *deal.II Differential Equations Analysis Library, Technical Reference*, 2016. <http://www.dealii.org>.
- [8] Y. Bazilevs, K. Takizawa, and T. Tezduyar. *Computational Fluid-Structure Interaction: Methods and Applications*. Wiley, 2013.
- [9] M. J. Borden, C. V. Verhoosel, M. A. Scott, T. J. R. Hughes, and C. M. Landis. A phase-field description of dynamic brittle fracture. *Comput. Meth. Appl. Mech. Engrg.*, 217:77–95, 2012.
- [10] B. Bourdin. Numerical implementation of the variational formulation for quasi-static brittle fracture. *Interfaces and free boundaries*, 9:411–430, 2007.
- [11] B. Bourdin, G. Francfort, and J.-J. Marigo. Numerical experiments in revisited brittle fracture. *J. Mech. Phys. Solids*, 48(4):797–826, 2000.
- [12] B. Bourdin, G. Francfort, and J.-J. Marigo. The variational approach to fracture. *J. Elasticity*, 91(1–3):1–148, 2008.
- [13] B. Bourdin, C. Larsen, and C. Richardson. A time-discrete model for dynamic fracture based on crack regularization. *Int. J. Frac.*, 168(2):133–143, 2011.
- [14] A. Braides. *Approximation of free-discontinuity problems*. Springer Berlin Heidelberg, 1998.
- [15] M. Bukac, S. Canic, R. Glowinski, B. Muha, and A. Quaini. A modular, operator-splitting scheme for fluid-structure interaction problems with thick structures. *International Journal for Numerical Methods in Fluids*, 74(8):577–604, 2014.
- [16] H.-J. Bungartz, M. Mehl, and M. Schäfer. *Fluid-Structure Interaction II: Modelling, Simulation, Optimization*. Lecture Notes in Computational Science and Engineering. Springer, 2010.
- [17] H.-J. Bungartz and M. Schäfer. *Fluid-Structure Interaction: Modelling, Simulation, Optimization*, volume 53 of *Lecture Notes in Computational Science and Engineering*. Springer, 2006.
- [18] S. Burke, C. Ortner, and E. Süli. An adaptive finite element approximation of a variational model of brittle fracture. *SIAM J. Numer. Anal.*, 48(3):980–1012, 2010.
- [19] P. Causin, J.-F. Gerbeau, and F. Nobile. Added-mass effect in the design of partitioned algorithms for fluid-structure problems. *Comput. Methods Appl. Mech. Engrg.*, 194:4506–4527, 2005.
- [20] P. G. Ciarlet. *Mathematical Elasticity. Volume 1: Three Dimensional Elasticity*. North-Holland, 1984.

- [21] G. dal Maso, G. A. Francfort, and R. Toader. Quasistatic crack growth in nonlinear elasticity. *Arch. Ration. Mech. Anal.*, 176:165–225, 2005.
- [22] R. Dautray and J.-L. Lions. *Mathematical Analysis and Numerical Methods for Science and Technology*, volume 5. Springer-Verlag, Berlin-Heidelberg, 2000.
- [23] T. A. Davis and I. S. Duff. An unsymmetric-pattern multifrontal method for sparse LU factorization. *SIAM J. Matrix Anal. Appl.*, 18(1):140–158, 1997.
- [24] P. Deuflhard. *Newton Methods for Nonlinear Problems*, volume 35 of *Springer Series in Computational Mathematics*. Springer Berlin Heidelberg, 2011.
- [25] J. Donea, P. Fasoli-Stella, and S. Giuliani. Lagrangian and Eulerian finite element techniques for transient fluid-structure interaction problems. In *Trans. 4th Int. Conf. on Structural Mechanics in Reactor Technology*, page Paper B1/2, 1977.
- [26] J. Donea, A. Huerta, J.-P. Ponthot, and A. Rodriguez-Ferran. *Arbitrary Lagrangian-Eulerian methods*, pages 1–25. Encyclopedia of Computational Mechanics. John Wiley and Sons, 2004.
- [27] T. Dunne. *Adaptive Finite Element Approximation of Fluid-Structure Interaction Based on Eulerian and Arbitrary Lagrangian-Eulerian Variational Formulations*. PhD thesis, University of Heidelberg, 2007.
- [28] T. Dunne, T. Richter, and R. Rannacher. *Numerical simulation of fluid-structure interaction based on monolithic variational formulations*, pages 1–75. Contemporary Challenges in Mathematical Fluid Mechanics. Springer, World Scientific, Singapore, 2010.
- [29] L. C. Evans. *Partial differential equations*. American Mathematical Society, 2000.
- [30] M. Fernández and J.-F. Gerbeau. *Algorithms for fluid-structure interaction problems*, pages 307–346. Volume 1 of Formaggia et al. [33], 2009.
- [31] M. A. Fernandez and J. Mullaert. Displacement-velocity correction schemes for incompressible fluid-structure interaction. *Comptes Rendus Mathematique*, 349(17):1011 – 1015, 2011.
- [32] L. Formaggia and F. Nobile. A stability analysis for the arbitrary Lagrangian Eulerian formulation with finite elements. *East-West Journal of Numerical Mathematics*, 7:105 – 132, 1999.
- [33] L. Formaggia, A. Quarteroni, and A. Veneziani. *Cardiovascular Mathematics: Modeling and simulation of the circulatory system*. Springer-Verlag, Italia, Milano, 2009.
- [34] M. Fortin and R. Glowinski. *Augmented Lagrangian Methods: Applications to the Numerical Solution of Boundary Value Problems*. Stud. Math. Appl. 15. North Holland, Amsterdam, 1983.
- [35] G. Francfort and J.-J. Marigo. Revisiting brittle fracture as an energy minimization problem. *J. Mech. Phys. Solids*, 46(8):1319–1342, 1998.
- [36] G. Galdi and R. Rannacher. *Fundamental Trends in Fluid-Structure Interaction*. World Scientific, 2010.
- [37] F. Gazzola and M. Squassina. Global solutions and finite time blow up for damped semilinear wave equations. *Ann. I. H. Poincaré*, 23:185–207, 2006.
- [38] T. Gerasimov and L. D. Lorenzis. A line search assisted monolithic approach for phase-field computing of brittle fracture. *Computer Methods in Applied Mechanics and Engineering*, pages –, 2015.
- [39] V. Girault and P.-A. Raviart. *Finite Element method for the Navier-Stokes equations*. Number 5 in Computer Series in Computational Mathematics. Springer-Verlag, 1986.
- [40] R. Glowinski and P. L. Tallec. *Augmented Lagrangian and Operator-Splitting Methods in Nonlinear Mechanics*. SIAM Stud. Appl. Math. 9. SIAM, Philadelphia, 1989.
- [41] H. Gomez and T. Hughes. Provably unconditionally stable, second-order time accurate, mixed variational methods for phase-field models. *Journal of Computational Physics*, 230:5310–5327, 2011.
- [42] A. A. Griffith. The phenomena of rupture and flow in solids. *Philos. Trans. R. Soc. Lond.*, 221:163–198, 1921.
- [43] T. Heister, M. F. Wheeler, and T. Wick. A primal-dual active set method and predictor-corrector mesh adaptivity for computing fracture propagation using a phase-field approach. *Comp. Meth. Appl. Mech. Engrg.*, 290(0):466 – 495, 2015.
- [44] B. Helenbrook. Mesh deformation using the biharmonic operator. *Int. J. Numer. Methods Engrg.*, pages 1–30, 2001.
- [45] J. G. Heywood and R. Rannacher. Finite-element approximation of the nonstationary Navier-Stokes problem part iv: Error analysis for second-order time discretization. *SIAM Journal on Numerical Analysis*, 27(2):353–384, 1990.
- [46] J. G. Heywood, R. Rannacher, and S. Turek. Artificial boundaries and flux and pressure conditions for the incompressible Navier-Stokes equations. *International Journal of Numerical Methods in Fluids*, 22:325–352, 1996.
- [47] C. Hirt, A. Amsden, and J. Cook. An arbitrary Lagrangian-Eulerian computing method for all flow speeds. *J. Comput. Phys.*, 14:227–253, 1974.
- [48] G. Holzapfel. *Nonlinear Solid Mechanics: A continuum approach for engineering*. John Wiley and Sons, LTD, 2000.
- [49] J. Hron and S. Turek. *A monolithic FEM/Multigrid solver for ALE formulation of fluid structure with application in biomechanics*, volume 53, pages 146–170. Springer-Verlag, 2006.
- [50] T. Hughes, W. Liu, and T. Zimmermann. Lagrangian-Eulerian finite element formulation for incompressible viscous flows. *Comput. Methods Appl. Mech. Engrg.*, 29:329–349, 1981.
- [51] C. J. Larsen. *IUTAM Symposium on Variational Concepts with Applications to the Mechanics of Materials: Proceedings of the IUTAM Symposium on Variational Concepts with Applications to the Mechanics of Materials, Bochum, Germany, September 22-26, 2008*, chapter Models for Dynamic Fracture Based on Griffith’s Criterion, pages 131–140. Springer Netherlands, Dordrecht, 2010.
- [52] C. J. Larsen, C. Ortner, and E. Süli. Existence of solutions to a regularized model of dynamics fracture. *Methods in Applied Sciences*, 20:1021–1048, 2010.
- [53] S. Lee, M. F. Wheeler, and T. Wick. Pressure and fluid-driven fracture propagation in porous media using an adaptive finite element phase field model. *Computer Methods in Applied Mechanics and Engineering*, 305:111 – 132, 2016.
- [54] M. Luskin and R. Rannacher. On the soothng property of the Crank-Nicolson scheme. *Applicable Analysis*, 14(2):117 – 135, 1982.
- [55] C. Miehe, M. Hofacker, L.-M. Schaenzel, and F. Aldakheel. Phase field modeling of fracture in multi-physics problems. part ii. coupled brittle-to-ductile failure criteria and crack propagation in thermo-elastic-plastic solids. *Computer Methods in Applied Mechanics and Engineering*, 294:486 – 522, 2015.
- [56] C. Miehe, M. Hofacker, and F. Welschinger. A phase field model for rate-independent crack propagation: Robust algorithmic implementation

- based on operator splits. *Comput. Meth. Appl. Mech. Engrg.*, 199:2765–2778, 2010.
- [57] C. Miehe, S. Mauthe, and S. Teichtmeister. Minimization principles for the coupled problem of darcy-biot-type fluid transport in porous media linked to phase field modeling of fracture. *Journal of the Mechanics and Physics of Solids*, 82:186 – 217, 2015.
- [58] C. Miehe, L.-M. Schaenzel, and H. Ulmer. Phase field modeling of fracture in multi-physics problems. part i. balance of crack surface and failure criteria for brittle crack propagation in thermo-elastic solids. *Computer Methods in Applied Mechanics and Engineering*, 294:449 – 485, 2015.
- [59] C. Miehe, F. Welschinger, and M. Hofacker. Thermodynamically consistent phase-field models of fracture: variational principles and multi-field fe implementations. *Int. J. Numer. Methods Engrg.*, 83:1273–1311, 2010.
- [60] A. Mikelić, M. F. Wheeler, and T. Wick. A phase-field method for propagating fluid-filled fractures coupled to a surrounding porous medium. *SIAM Multiscale Model. Simul.*, 13(1):367–398, 2015.
- [61] A. Mikelić, M. F. Wheeler, and T. Wick. Phase-field modeling of a fluid-driven fracture in a poroelastic medium. *Computational Geosciences*, 19(6):1171–1195, 2015.
- [62] A. Mikelić, M. F. Wheeler, and T. Wick. A quasi-static phase-field approach to pressurized fractures. *Nonlinearity*, 28(5):1371–1399, 2015.
- [63] W. Noh. *A time-dependent two-space-dimensional coupled Eulerian-Lagrangian code*, volume 3 of *Methods Comput. Phys.*, pages 117–179. Academic Press, New York, 1964.
- [64] R. Rannacher. Finite element solution of diffusion problems with irregular data. *Numer. Math.*, 43:309–327, 1984.
- [65] R. Rannacher. On the stabilization of the Crank-Nicolson scheme for long time calculations. Preprint, August 1986.
- [66] R. Rannacher. Finite element methods for the incompressible Navier-Stokes equations. Lecture notes, August 1999.
- [67] J. Rice. *Mathematical analysis in the mechanics of fracture*, pages 191–311. Academic Press New York, chapter 3 of fracture: an advanced treatise edition, 1968.
- [68] T. Richter and T. Wick. Finite elements for fluid-structure interaction in ALE and fully Eulerian coordinates. *Comp. Methods Appl. Mech. Engrg.*, 199:2633–2642, 2010.
- [69] T. Richter and T. Wick. On time discretizations of fluid-structure interactions. In T. Carraro, M. Geiger, S. Körkel, and R. Rannacher, editors, *Multiple Shooting and Time Domain Decomposition Methods*, pages 377–400, Contributions in Mathematical and Computational Science, 2015.
- [70] P. Schreurs. Fracture mechanics. Lecture notes course 4A780, Eindhoven University of Technology, 2012.
- [71] I. N. Sneddon and M. Lowengrub. *Crack problems in the classical theory of elasticity*. SIAM series in Applied Mathematics. John Wiley and Sons, Philadelphia, 1969.
- [72] K. Stein, T. Tezduyar, and R. Benney. Mesh moving techniques for fluid-structure interactions with large displacements. *J. Appl. Mech.*, 70:58–63, 2003.
- [73] M. Wheeler, T. Wick, and W. Wollner. An augmented-Lagangian method for the phase-field approach for pressurized fractures. *Comp. Meth. Appl. Mech. Engrg.*, 271:69–85, 2014.
- [74] T. Wick. Fluid-structure interactions using different mesh motion techniques. *Computers and Structures*, 89(13-14):1456–1467, 2011.
- [75] T. Wick. Solving monolithic fluid-structure interaction problems in arbitrary Lagrangian Eulerian coordinates with the deal.II library. *Archive of Numerical Software*, 1:1–19, 2013.
- [76] T. Wick. Modeling, discretization, optimization, and simulation of fluid-structure interaction. Lecture notes at Heidelberg University, TU Munich, and JKU Linz available on <https://www-m17.ma.tum.de/Lehrstuhl/LehreSoSe15NMFSIEn>, 2015.
- [77] T. Wick. Coupling fluid-structure interaction with phase-field fracture: modeling and a numerical example. RICAM preprint No. 2015-22, accepted for publication in Numerical Mathematics and Advanced Applications, Proceedings of ENUMATH 2015, Feb 2016.
- [78] T. Wick. An error-oriented newton/inexact augmented lagrangian approach for fully monolithic phase-field fracture propagation. RICAM Preprint No. 2016-13 at <http://www.ricam.oeaw.ac.at/publications/reports/>, 2016.
- [79] T. Wick. Goal functional evaluations for phase-field fracture using pu-based dwr mesh adaptivity. *Computational Mechanics*, pages 1–19, 2016.
- [80] T. Wick, G. Singh, and M. Wheeler. Fluid-filled fracture propagation using a phase-field approach and coupling to a reservoir simulator. *SPE Journal*, pages 1–19, 2015.
- [81] J. Wloka. *Partielle Differentialgleichungen*. B. G. Teubner Verlag, Stuttgart, 1982.
- [82] X. P. Xu and A. Needleman. Numerical simulations of fast crack growth in brittle solids. *J. Mech. Phys. Solids*, 42:1397–1434, 1994.